Journal of Nanobiotechnology

RESEARCH

Open Access

Sequentially assembled co-delivery nanoplatform of SIRT1 protein and SOX9-expressing plasmid for multipronged therapy of intervertebral disc degeneration

Xiaoyu Zhang[1†], Qianping Guo[1†], Jiawei Fang[1†], Qi Cheng[1], Zhuang Zhu[1], Qifan Yu[1], Huan Wang[1], Youzhi Hong[1], Chengyuan Liu[1], Huilin Yang[1], Caihong Zhu[1*], Bin Li[1*] and Li Ni[1*]

Abstract

Nucleus pulposus cells (NPCs) undergo metabolic disorders and matrix pathological remodeling under the influence of various adverse factors during intervertebral disc degeneration (IVDD), whereas post-translational modifications (PTMs) can confer cells with the capacity to respond quickly and adapt to complex environmental changes. Here, SIRT1 protein, a key regulator within PTMs framework, was applied against the hostile degenerative microenvironment. Then, it was sequentially assembled with SOX9-expressing plasmid, an essential transcription factor to promote extracellular matrix (ECM) biosynthesis, onto a phenylboronic acid-functionalized G5-dendrimer to construct a multifunctional nanoplatform for IVDD therapy. In vitro, the nanoplatforms showed antioxidant capacity, and the ability to restore mitochondrial homeostasis and normal ECM metabolism, as well as to maintain cellular phenotypes. RNA sequencing suggested that inhibition of the Nod-like receptor signaling might be the mechanism behind their therapeutic effects. The nanoplatforms were then wrapped in a designed dynamic hydrogel, not only prolonging the retention time of the loaded cargoes, but also well maintaining the disc structure, height, and water content in vivo. Overall, this study presents a convenient assembled strategy to inhibit the multiple adverse factors, and hold promise for the IVDD treatment.

†Xiaoyu Zhang, Qianping Guo and Jiawei Fang contributed equally to this work.

*Correspondence:
Caihong Zhu
zhucaihong@suda.edu.cn
Bin Li
binli@suda.edu.cn
Li Ni
nili@suda.edu.cn

Full list of author information is available at the end of the article

Graphical abstract

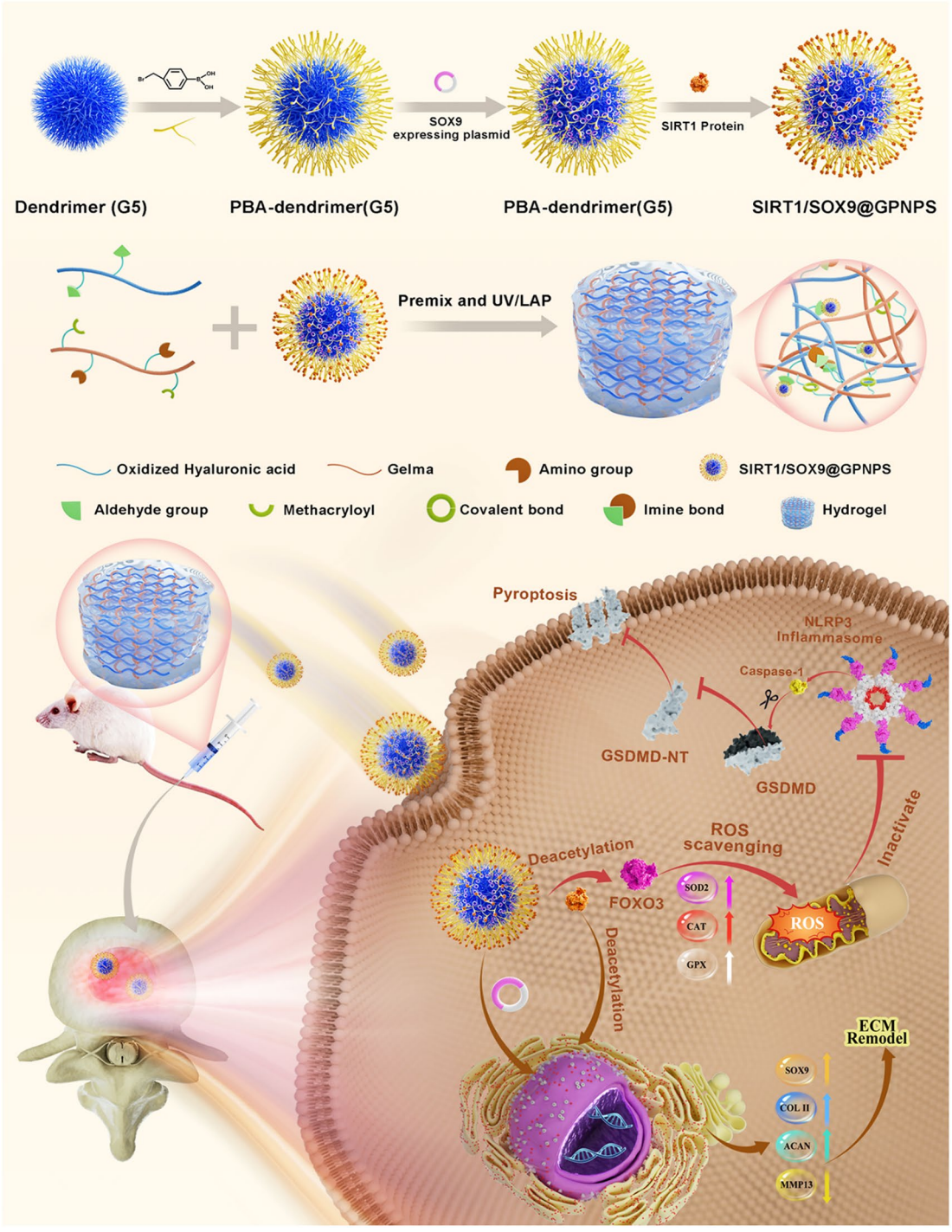

Keywords Sequentially assembled nanoplatform, Co-delivery, Post-translational modifications, Mitochondrial homeostasis, Intervertebral disc degeneration

Introduction

Low back pain (LBP) is a global challenge, and the burden of disease insidiously affects years lived with disability [1]. IVDD is the main contributor to chronic LBP, accounting for approximately 26–42% of cases [2]. Therefore, in clinical settings, intervening in the IVDD process through drugs, biological, or physical therapy has become common ways to relieve LBP symptoms [3].

The intervertebral disc (IVD) exhibits restricted repair capacity due to the lack of effective blood supply, rendering it vulnerable to adverse factors [4, 5]. The malignant transformation of the IVD microenvironment is reflected in the pathological changes experienced by NPCs, characterized by metabolic disorders and ECM remodeling [6]. These processes are marked by persistent oxidative stress, mitochondrial homeostasis imbalance, and matrix metabolic dysregulation [7]. When the cellular antioxidant defence system collapses, the accumulation of reactive oxygen species (ROS) overwhelms the mitochondrial structure and damages key functional molecules, leading to mitochondrial homeostasis imbalance [8]. Under conditions of excessive ROS and inflammatory responses, NPCs undergo disruptions in both anabolic and catabolic matrix metabolism, exacerbating the loss of cellular function [9]. Methods have been developed to promote metabolic balance by regulating metabolic enzyme expression, controlling substrate concentrations, and facilitating PTMs of related proteins [10]. PTMs unveil the rich connotation of post-translational events and protein interactions, elucidating the precise interaction between proteins and multi-modular biological processes [11, 12]. Compared to the conventional promotion of de novo protein synthesis, PTMs offer the advantage of rapid dynamic regulation when cells face adverse conditions [13]. Additionally, most PTMs possess reversible equilibrium mechanisms, which allow cells to respond flexibly to changes in the internal and external environment, thereby maintaining physiological homeostasis [14]. Hence, PTM-based strategies are expected to show promising potential in the treatment of IVDD by antagonizing the multiple adverse factors faced by IVD cells.

Sirtuin 1 (SIRT1), a highly conserved NAD-dependent deacetylase, has emerged as a critical regulator within the framework of PTMs [15]. By regulating the acetylation status of a diverse array of proteins, SIRT1 influences key physiological and pathological pathways. SIRT1 and FOXO3 form a complex in cells and deacetylate FOXO3 to increase the activity levels of several antioxidant enzymes [16, 17]. SIRT1 enhances antioxidant responses, reconstructs the damaged mitochondrial homeostasis, and promotes cellular resistance to adverse factors [18]. The inhibition of ECM catabolism is driven by SIRT1, and the inactivation thereof decreases the stability of the ECM by activating matrix metalloproteinases (MMPs) [19].

However, the gradual loss of the ECM is caused by the variable adverse microenvironment in IVDD [20]. Although SIRT1 has demonstrated its powerful function as a therapeutic factor, it remains challenging for fighting against complex pathogenic factors by relying on a single therapeutic intervention [21]. Sex Determining Region Y Box Protein 9 (SOX9) is widely applied in the biosynthesis and maintenance of ECM [22]. By promoting the expression of COL II (Collagen type II) and ACAN (Aggrecan), SOX9 safeguards the integrity and functionality of the ECM [23]. However, SOX9 is sensitive to the inflammatory microenvironment, where various cytokines can induce the loss of SOX9 by inhibiting the TGF-β/Smad signaling pathways; if left unchecked, this process can lead to sustained damage of the ECM [24]. The therapeutic effect of SIRT1 may be limited by the absence of SOX9, and the upregulation of SOX9 can enhance the positive production of endogenous ECM as a compensatory mechanism. Synergistic cooperation between SIRT1 and SOX9 may improve IVD cell function, and upregulation of the protein levels of SIRT and SOX9 via tissue engineering shows great potential for IVDD therapy.

Strategies to promoting target protein expression include recombinant plasmids construction, intracellular delivery of proteins, and RNA interference (RNAi) [25, 26]. Protein-based therapeutics are attracting increasing attention for their potential in the treatment of IVDD. However, current therapies focus on extracellular targets, such as TGF-β1, SDF-1α, and IL-1ra [27, 28]. Due to their poor cell membrane permeability, intracellular proteins have not been widely applied [29], and choosing suitable carriers is necessary and poses a considerable challenge. Gene therapy has also been well received. Plasmids, characterized by their circular DNA structures, offer exceptional stability [30]. However, effective plasmid delivery also depends on the availability of carriers. Combination therapy via the nanocarrier-based co-delivery strategy has attracted increased attention because this strategy enables different agents to be delivered to the same target cells, thus achieving more exciting effects [31, 32]. For example, a lipid/GNs-based vehicle successfully delivered Cas9 protein and sgRNA plasmid simultaneously to tumor cells and tissues, inhibiting tumor progression with high efficiency [33]. However, to maximize combinational effects, a sequential delivery system is required to realize unique targets of different loaded cargoes. Chen et al. developed a liposome-based nanoassembly that could progressively load with a plasmid DNA encoding tumor-suppressing p53 protein (p53 DNA) and with an apoptotic protein cytochrome c (CytoC), enabling their sequential delivery to specific intracellular sites,

thereby significantly enhancing apoptosis and inhibiting tumor growth [34]. The delivery of protein and plasmid into cells exhibits time-sequential characteristics in therapeutic effects. Generally, the delivered protein into cytoplasm targets direct action points, while the delivered plasmid goes a series of processes into nucleus to continuously express functional proteins [35, 36]. This time-sequential action offers us a promising programmable therapeutic co-delivery strategy to meet the procedural needs of IVDD repair, with SIRT1 protein delivered into the cytoplasm to improve the hostile microenvironment first, and SOX9-overexpressing plasmid delivered to the nucleus of the same cell to promote ECM secretion.

Recently, a phenylboronic acid-functionalized G5-dendrimer (G5-PBA-dendrimer) was developed [37]. Compared to other nanodelivery platforms, the G5-dendrimer with a monodisperse hyperbranched structure possesses significantly enhanced drug-loading capacity due to its dendritic termini containing abundant active sites [38]. Thus, It has been extensively explored for its applications, particularly in the field of bioactive factor delivery for therapeutic purposes. Furthermore, due to its abundant density of boronic acid groups, benzene rings, and cationic units, it can load proteins through the form of nitrogen-boronate coordination between phenylboronic acid groups and proteins, and encapsulate genes through ionic interactions. The G5-PBA-dendrimers can deliver saporin or p65 siRNA into osteosarcoma cells or NPCs, respectively, and performs the biological function thereof [39, 40]. Here, we aimed to engineer a nanoassembly strategy to sequentially co-deliver SIRT1 protein and SOX9-expressing plasmid for the therapy of IVDD. SOX9-expressing plasmid was first compressed by cationic G5-PBA-dendrimers nanoplatforms (GPNPs) via ionic interactions (SOX9@GPNPs) and, subsequently, SIRT1 protein was further loaded via nitrogen-boronate coordination (SIRT1/SOX9@GPNPs) (Scheme 1). All the nanocomplexes showed high delivery efficiency. To validate the biological functions of SIRT1/SOX9@GPNPs, this study conducted a series of in vitro experiments to investigate their effects on oxidative stress, mitochondrial function, apoptosis, cellular phenotypes, and the balance between ECM anabolism and catabolism. Based on RNA-seq analysis, we further explored the underlying molecular mechanisms by which SIRT1/SOX9@GPNPs regulate multiple biological functions of NPCs. Furthermore, to enhance the in vivo therapeutic efficacy of SIRT1/SOX9@GPNPs, we developed a composite hydrogel to achieve sustained release of SIRT1/SOX9@GPNPs and maintain prolonged therapeutic effects in a cultured model. Finally, the efficacy of the composite hydrogel was evaluated in a rat model of intervertebral disc degeneration.

Results

Preparation and characterization of nanoplatforms for co-delivery of SIRT1 protein and SOX9-expressing plasmid

First, according to methods previously reported, the boronic acid-rich dendrimer were prepared through the modification of amino termini of a generation 5 polyamidoamine (G5-PAMAM) with phenylboronic acid (PBA). ^{1}H NMR analysis is used to analyse the structure of organic compounds, and results indicated that approximately 65 amino groups per G5-dendrimer were converted to PBA, and this substituted dendrimer was previously reported to have the highest protein and gene delivery efficiency, labeled as G5-PBA-dendrimer nanoplatforms (GPNPs) (Additional file 1: Figure S1). Then, to verify the potent delivery capability of GPNPs for the SOX9-expressing plasmid and complex stability, agarose gel electrophoresis at various n/p ratios were tested and showed that GPNPs could form stable complexes with plasmid, even at an n/p ratio of 1/1 (Additional file 1: Figure S2). The zeta potential revealed that GPNPs changed the plasmid charge state from negative to positive at N/P ratios of greater than 2:1 (Additional file 1: Figure S3). Subsequently, the formed complexes of the pcDNA3.1-Sox9-ZsGreen1, which has gene fragments for fluorescent protein expression with GPNPs at different n/p ratios, were found to result in ZFgreen1-positive cells after transfection. Furthermore, with the increase of the n/p ratio, the number of ZFgreen1-positive cells gradually increased; however, this led to an increase in cytotoxicity (Additional file 1: Figure S4, S5). Thus, to balance optimal transfection efficiency and minimal cytotoxicity, an n/p ratio of 8:1 was selected as the ideal proportion for subsequent experiments. The obtained complex of SOX9-expressing plasmid with GPNPs (SOX9@GPNPs) had a diameter at approximately 270 nm (Fig. 1A), and the intracellular ZsGreen1 expression level was high at this point after delivery (Fig. 1B). Further, the biological function of SOX9 on NPCs after SOX9@GPNPs transfection was verified by qRT-PCR, and the results showed that the expression levels of ECM-related characteristic genes (*Sox9*, *Col2a1* and *Acan*) were significantly increased compared with the control (Fig. 1C).

SIRT1 protein was then loaded onto GPNPs, and it was found that nanoparticles could be formed at various mass ratios and that all exhibited good biocompatibility (Additional file 1: Figure S6). Nanoparticle diameter usually affects cellular uptake rates; hence, a mass ratio of 2:1 was used for follow-up experiments to form the nanoplatform (SIRT1@GNPNs) with a diameter at approximately 150 nm (Fig. 1D). Additionally, to verify the protein delivery capability of GPNPs, BSA-FITC was used as a model protein. The results showed that BSA-FITC were effectively delivered into NPCs, and the green fluorescence of BSA-FITC was mainly localized in the cytoplasm, as

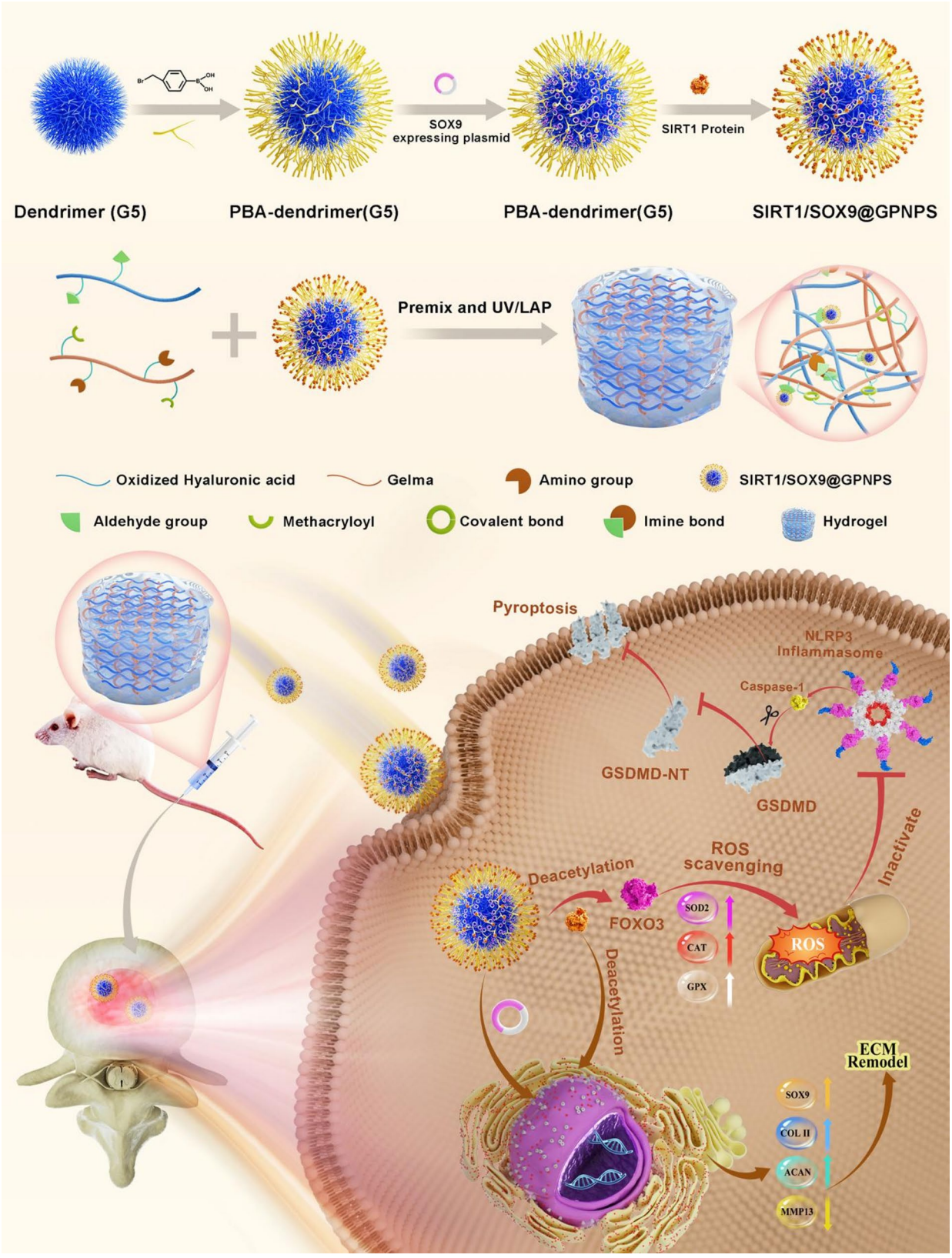

Scheme 1 Schematic illustration of the sequentially assembled nanoplatform for IVDD repair

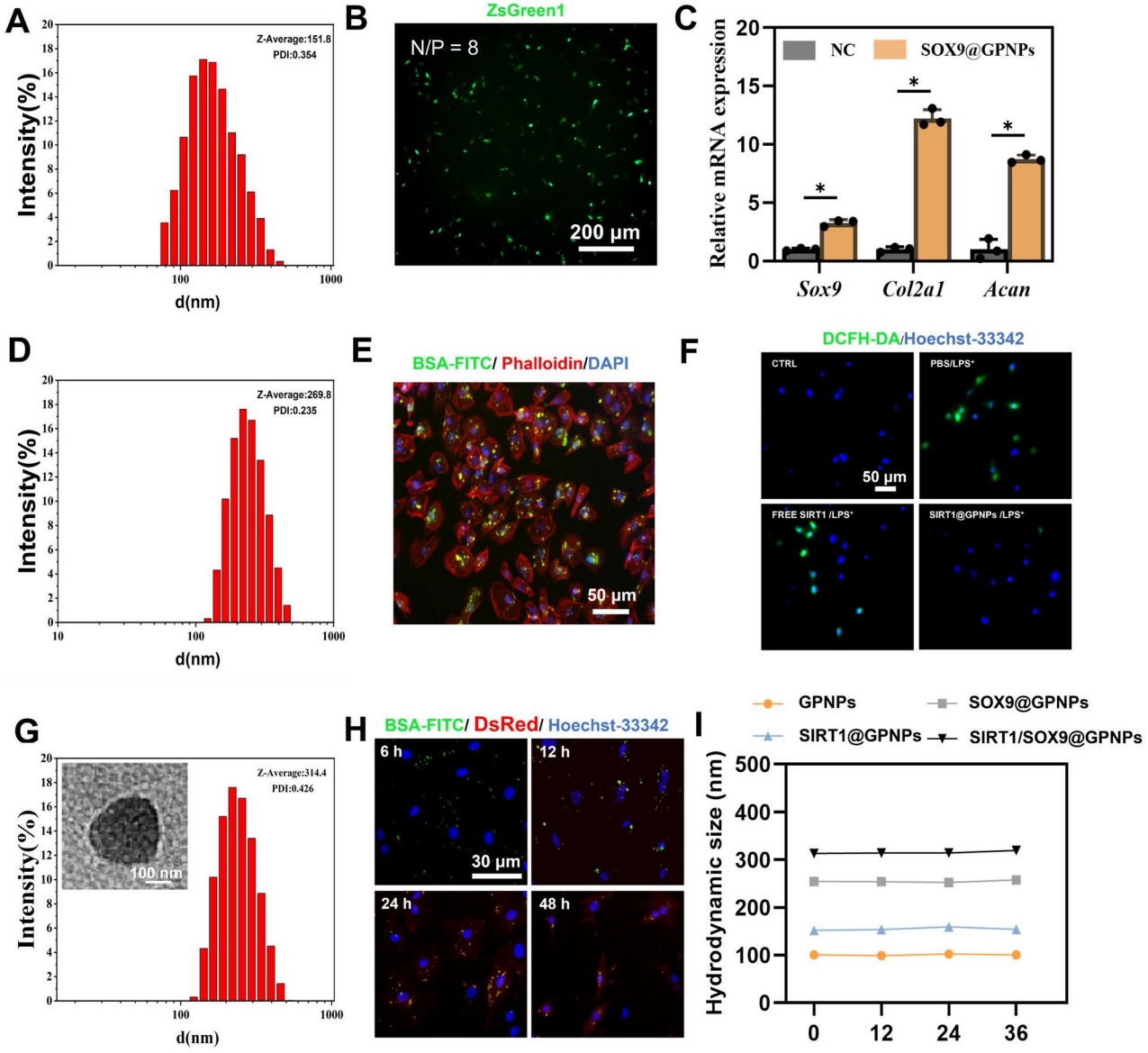

Fig. 1 Preparation and characterization of SOX9@GPNPs, SIRT1@GPNPs and SOX9/SIRT1@GPNPs. (**A**) Particle size of SOX9@GPNPs. (**B**) Transfection efficiency of pcDNA3.1-Sox9-ZsGreen1 at an n/p ratio of 8:1. (**C**) By qRT-PCR quantifications of gene expression (*Sox9*, *Col2a1* and *Acan*) at an n/p ratio of 8:1 ($n=3$). (**D**) Particle size of SIRT1@GPNPs. (**E**) Fluorescent images of NPCs treated with BSA-FITC@GPNPs for 6 h, and the cellular cytoskeletons were stained by phalloidin-rhodamine. (**F**) Representative images of ROS staining (green) for NPCs, as co-cultured with PBS, PBS/LPS$^+$, FREE SIRT1/LPS$^+$, and SIRT1@GPNPs/LPS$^+$. (**G**) Particle size of SIRT1/SOX9@GPNPs via DLS and TEM. (**H**) Fluorescence imaging of pcDNA3.1-Sox9-DsRed and BSA-FITC at different time points after the nanoplatform-mediated delivery. (**I**) The particle sizes of GPNPs, SOX9@GPNPs, and SIRT1/SOX9@GPNPs measured at 0, 12, 24, and 36 h after preparation ($n=3$). Data are presented as mean ± SD. $^*p<0.05$; ns, no significant difference. Statistical significance was determined by one-way ANOVA with a post-hocTukey test for (**C**). ZsGreen1, green fluorescent protein encoded by pcDNA3.1-Sox9-ZsGreen1 for the assessment of plasmid transfection efficiency; NC group, with no *Sox9* expression; SOX9@GPNPs, with *Sox9* expression; BSA-FITC, FITC-labeled BSA with green fluorescence; Phalloidin, rhodamine-labeled phalloidin staining solution; DCFH-DA, green fluorescent probe for ROS detection; DsRed, red fluorescent protein encoded by pcDNA3.1-Sox9-DsRed for the assessment of plasmid transfection efficiency; GPNPs, PBA-modified G5-dendrimers; SOX9@GPNPs, GPNPs loaded with SOX9-expressing plasmid; SIRT1@GPNPs, GPNPs loaded with SIRT1 proteins; SIRT1/SOX9@GPNPs, GPNPs assembled sequentially with SOX9- expressing plasmid and SIRT1 protein

indicated by red fluorescence stained with phalloidin. A few BSA-FITC was also found to distribute in nucleus, indicating that GPNPs possess nuclear delivery capabilities (Fig. 1E). Then, the biological function of SIRT1 protein delivered by the nanoplatform SIRT1@GNPNs on NPCs was evaluated. LPS (Lipopolysaccharides) has been demonstrated to promote redox homeostasis imbalance, mitochondrial dysfunction, and apoptosis by inducing an oxidative stress microenvironment [41]. In several studies, the LPS-induced oxidative stress model

has been utilized as nucleus pulposus cells degeneration model and applied in the evaluation of therapeutic strategies [7, 21]. Due to these effects, LPS is widely employed in research to replicate the inflammatory and oxidative stress environment characteristic of IVDD in vitro. And during this process, a surge of ROS is produced, leading to cellular and mitochondrial damage. Given this, ROS detection serves as a critical indicator of SIRT1 biological function. Through the test of a DCFH-DA fluorescent probe, which reflects intracellular ROS levels in NPCs, it was found that the intervention of free SIRT1 did not significantly change the level of ROS induced by LPS; however, SIRT1@GNPNs group could effectively control the level of ROS (Fig. 1F). This clearly suggested that free SIRT1 has difficulty penetrating cell membranes and exerting biological functions, whereas the dendrimer nanoplatform is appropriate for SIRT1 protein delivery.

Based on the timing requirements of repair in IVDD, it is hoped that SIRT1 can rapidly improve the adverse cell microenvironment and then maximize the function of SOX9 to promote ECM expression. We tried to load SOX9-expressing plasmid on GNPNs first, and then SIRT1 protein into the same nanoparticle to achieve their co-delivery in the same cell. As shown in Fig. 1G, it was found that an engineered nanoplatform labeled SIRT1/SOX9@GPNPs was successfully assembled with a diameter of approximately 315 nm, although its dimension was slightly larger than that of nanoparticles loaded with SIRT1 protein or SOX9-expressing plasmid alone. Zeta potential shows that the surface potential of the nanocomplex formed after sequential assembly of SOX9 expression plasmid and SIRT1 protein remains positively charged (Additional file 1: Figure S7). Fluorescence imaging indicated that in the initial 6 h, only green fluorescence of protein was observed in the cells, while red fluorescence expressed by plasmid was absent. In 12 h post-transfection, green fluorescence of protein was predominantly observed in the cells, with minimal expression of SOX9 as indicated by red fluorescence, whereas after 24 h post-transfection, both red and green fluorescence were prominently expressed, suggesting that during the early stages, the protein may perform the primary function, and then the protein and plasmid play a role at the same time, which is exactly the same as the predicted effect (Fig. 1H). Thereafter, the stability of nanocomplexes including GPNPs, SOX9@GPNPs, SIRT1@GPNPs, and SIRT1/SOX9@GPNPs were monitored through DLS measurements, and the results showed that all the particles were stable and their sizes remained unchanged for over 36 h (Fig. 1I). The above results indicated that the SIRT1 protein and SOX9-expressing plasmid were successfully co-loaded onto the GPNPs, and could be effectively transferred into NPCs to perform biological functions.

Enhancing antioxidative capability and restoring mitochondrial homeostasis via the intervention of functional nanoplatform

Oxidative stress induced by factors such as LPS is one of critical factors in the initiation and progression of IVDD [42]. The antioxidant defence system is primarily composed of various antioxidant enzymes, including SOD, CAT, and GPX, which protect cells from oxidative damage by reducing superoxide levels, thereby restoring mitochondrial homeostasis [43]. Moreover, it has been shown that SIRT1-mediated deacetylation enhances FOXO3 transcriptional activity and regulates its subcellular localization, thus inhibiting oxidative stress in rats [44]. To test the therapeutic effects of the functional nanoplatform, five experimental groups co-cultured with NPCs were established under the treatment of LPS. Results of qRT-PCR showed that LPS treatment significantly downregulated the expression levels of antioxidant genes FOXO3, CAT, SOD2, and GPX in NPCs, indicating an impaired antioxidant defence system. SOX9@GPNPs had a limited effect on the rescue of antioxidant function in NPCs, while SIRT1@GPNPs and SIRT1/SOX9@GPNPs significantly upregulated the expression levels of FOXO3 and antioxidant genes (Fig. 2A), indicating that SIRT1 was responsible for the improvement of antioxidant capacity. Correspondingly, compared to the PBS group, SOX9@GPNPs treatment did not mitigate the high level of ROS induced by LPS. In contrast, other groups showed different results. The interventions of SIRT1@GPNPs and SIRT1/SOX9@GPNPs significantly reduced the green fluorescence intensity of DCFH-DA (Fig. 2B).

Restoration of mitochondrial homeostasis has emerged as a key strategy to defend against multiple adverse factors, including ROS [45]. To estimate the regulation of GPNPs on mitochondrial homeostasis, a MitoSOX assay was conducted to measure the superoxide production in mitochondria. As expected, the intensity of LPS-induced red fluorescence was also significantly inhibited by SIRT1@GPNPs and SIRT1/SOX9@GPNPs, but not SOX9@GPNPs (Fig. 2C). Furthermore, JC-1 staining is used to assess mitochondrial membrane potential. Mitochondrial membrane potential was largely restored in both the SIRT1@GPNPs and SIRT1/SOX9@GPNPs groups, which was indicated by an increased red/green ratio (Fig. 2D). These fluorescence staining and quantitative analysis results were consistent, and no significant difference between the SIRT1@GPNPs group and SIRT1/SOX9@GPNPs group was found, which suggests that SIRT1 played a principal role in recovering mitochondrial stability. Mitochondrial morphology serves as a more direct and crucial assessment of mitochondrial homeostasis and function. Thus, we observed the mitochondrial morphology in different groups by using transmission

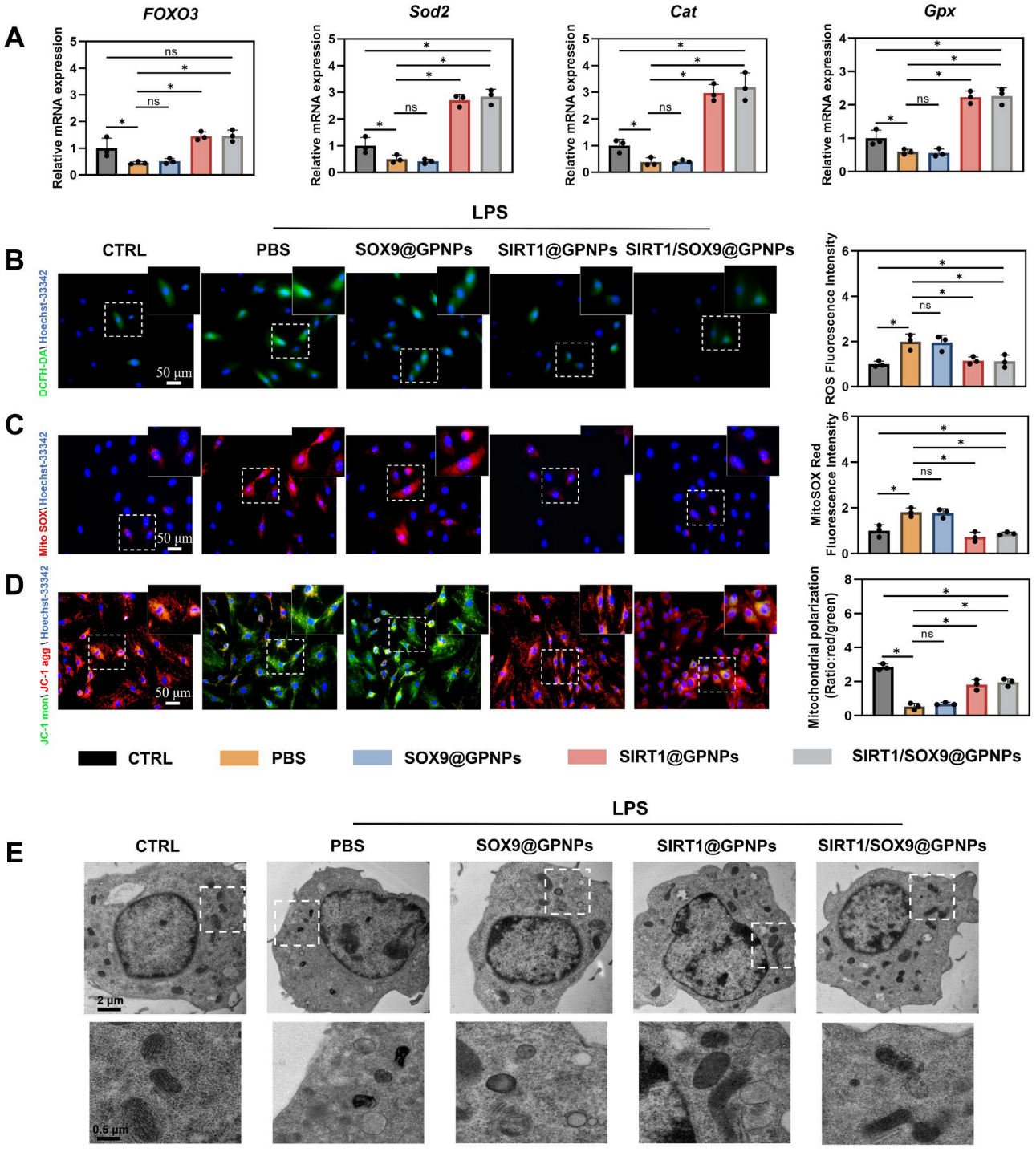

Fig. 2 Multifunctional nanodelivery platforms resist oxidative stress and restored mitochondrial homeostasis in NPCs. (**A**) Relative mRNA expression levels of *FOXO3*, *Sod2*, *Cat*, and *Gpx* genes ($n = 3$). Representative images and quantification of ROS staining (green, **B**), MitoSOX staining (red, **C**), and JC-1 staining (red/green fluorescent area, **D**) for NPCs, as co-cultured with PBS, SOX9@GPNPs, SIRT1@GPNPs, and SIRT1/SOX9@GPNPs ($n = 3$). (**E**) Representative TEM images of the mitochondria of NPCs. Data are presented as mean ± SD. $^{*}p < 0.05$; ns, no significant difference. Statistical significance was determined by one-way ANOVA with a post-hocTukey test for (**A**), (**B**), (**C**) and (**D**). GPNPs, PBA-modified G5-dendrimers; SOX9@GPNPs, GPNPs loaded with SOX9-expressing plasmid; SIRT1@GPNPs, GPNPs loaded with SIRT1 proteins; SIRT1/SOX9@GPNPs, GPNPs assembled sequentially with SOX9- expressing plasmid and SIRT1 protein; DCFH-DA, green fluorescent probe for ROS detection; Mito SOX, live-cell fluorescent probes targeting mitochondrial superoxide; JC-1, in normal mitochondria, JC-1 aggregates in the mitochondrial matrix, emitting strong red fluorescence. When the mitochondrial membrane potential is low, and JC-1 monomers emit green fluorescence

electron microscopy. Compared to the control group, LPS treatment led to the disappearance of vacuolization, mitochondrial cristae, and fewer mitochondrial numbers. In contrast, mitochondrial cristae and vacuolization were partly reversed in the SIRT1@GPNPs and SIRT1/SOX9@GPNPs groups, and mitochondrial numbers significantly increased (Fig. 2E).

Changes in mitochondrial permeability promote the activation of apoptosis-related proteins and the release of apoptosis-inducing factors, thereby driving mitochondria dependent apoptosis [46]. Flow cytometry was conducted to evaluate the effect of GPNPs on NPC activity and apoptosis. The control group showed 96.7% living cells and 1.7% apoptotic cells, after LPS induction; these numbers changed to 79.1% and 11.2%, respectively. Both SOX9@GPNPs and SIRT1@GPNPs groups showed improvement, with living and apoptotic cells at 85.2% and 6.2% for the former, and 87.8% and 5.8% for the latter (Additional file 1: Figure S8). ECM forms a supportive microenvironment for the function and growth of nucleus pulposus cells, which plays a critical role in regulating cellular behaviors, including proliferation, differentiation, and apoptosis. It has been demonstrated that correcting unfavorable growth microenvironments can enhance the viability of nucleus pulposus cells, thereby inhibiting apoptosis [6]. The improvement of cell apoptosis in the SOX9@GPNPs group may be attributed to the function of SOX9. At the same time, the protective effect of SIRT1 on mitochondria likely inhibited apoptosis in the SIRT1@GPNPs group. Notably, the SIRT1/SOX9@GPNPs group showed the best results, which indicated a strong synergistic anti-apoptotic capability.

Restoring the balance of ECM anabolism/catabolism via the intervention of functional nanoplatform

Disorders between the anabolism and catabolism of the ECM are also central to IVDD [47]. The aberrant expression of COL II, ACAN, and MMP13 usually disrupts ECM homeostasis. Additionally, abnormal expression of Cytokeratin 19 (KRT-19, a marker of NPCs) reveals phenotypic changes in NPCs [48]. Therefore, our subsequent experiments examined the influence on ECM metabolism and cell phenotype under different conditions. Western blot and quantification confirmed that SOX9@GPNPs and SIRT1@GPNPs reversed the decline in COL II and ACAN expression and the increase in MMP13 expression, which indicated improvement in the disordered metabolism of ECM synthesis and breakdown (Fig. 3A). Although the SIRT1@GPNPs group demonstrated a positive regulatory effect on ECM metabolism, the extent of this regulation was not as robust as that observed in the SOX9@GPNPs group, which suggested that SOX9@GPNPs play a more direct role in promoting ECM metabolic balance. Furthermore, the expression levels of COL II, ACAN, and MMP13 in the SIRT1/SOX9@GPNPs group were not statistically different from the control group, which indicated the synergistic effect of SIRT1 and SOX9 on ECM homeostasis of NPCs (Fig. 3A).

Consistent with the western blot results, immunofluorescence demonstrated that, compared to the control group, LPS treatment reduced the expression levels of COL II in NPCs. After treatment with SOX9@GPNPs and SIRT1/SOX9@GPNPs, the expression levels of COL II increased (Fig. 3B). Furthermore, the treatment of SIRT1/SOX9@GPNPs upregulated the expression of KRT-19, indicating the restoration of NPCs phenotype (Fig. 3C). Alcian Blue staining also confirmed that proteoglycan expression was significantly higher in the SIRT1/SOX9@GPNPs groups compared to the PBS group (Additional file 1: Figure S9). In summary, these results suggest that the SIRT1/SOX9@GPNPs can maintain ECM stability and the NPCs phenotype, and indicate that SIRT1 and SOX9 repair IVDD via synergistic cooperation. Hence, we further explored the molecular mechanism of the SIRT1/SOX9@GPNPs nanocomplex in the repair functions.

Signaling pathways underlying the therapeutic effect of the functional platform

To further explore the potential molecular mechanism in the functional platform therapy, we treated NPCs with LPS to induce inflammation and list information on the differential expression of genes upon addition of SIRT1/SOX9@GPNPs compared to treated NPCs with LPS alone. As shown in the volcano plot ($|\log2FC| \geq 1$ & $p < 0.05$), compared to PBS treatment, the treatment of SIRT1/SOX9@GPNPs resulted in the upregulation of 500 genes and the downregulation of 453 genes in NPCs (Fig. 4A). A heatmap analysis revealed significant differences in gene expression between the groups (Fig. 4B). Compared to LPS treatment, SIRT1/SOX9@GPNPs upregulated genes related to mitochondrial function maintenance, such as PCK2, GATM, and UCHL1. It also potentially inhibited the activation of cGAS through mitigating mitochondrial damage-induced mtDNA release. The metabolic balance of ECM is crucial for the maintenance of IVD functions. SIRT1/SOX9@GPNPs downregulated ECM degradation-related matrix metalloproteinases (MMP13, MMP3, ADAMTS7) and upregulated ECM synthesis-related genes (COL2A1, ACAN, TGFBR3, COL19A1, COL11A1, COL5A3, NPNT). Gene ontology (GO) analysis between the two groups suggested a strong correlation of DEGs with positive regulation of developmental process, positive regulation of defence response, and cell proliferation (Fig. 4C).

Notably, KEGG pathway enrichment analysis showed the downregulation of the NOD-like receptor signaling pathway (Fig. 4D). Moreover, gene set enrichment

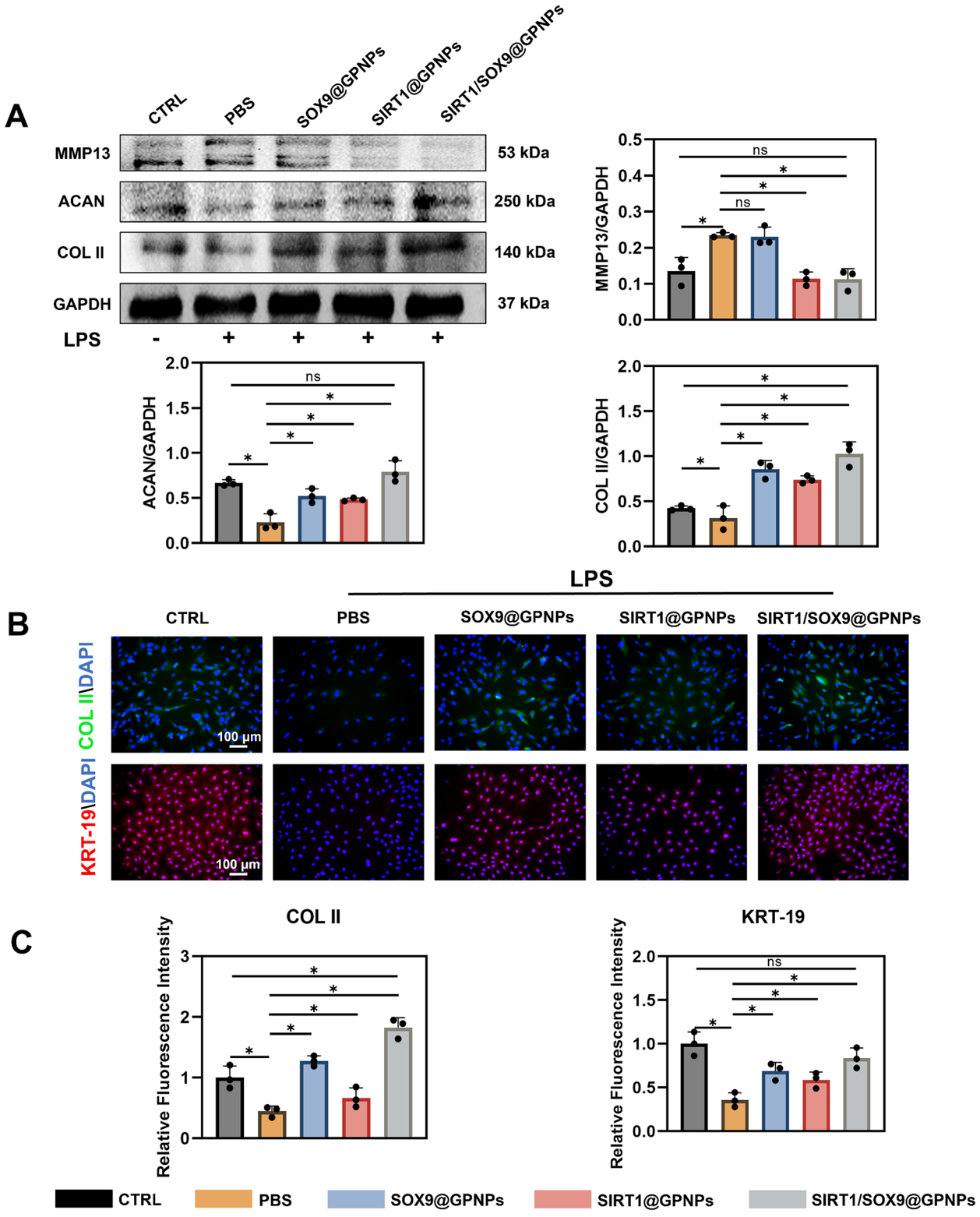

Fig. 3 The effect of multifunctional nanodelivery platforms to maintain ECM homeostasis balance and NPC phenotype. (**A**) Western blotting and quantitative analysis of MMP13, ACAN, and COL II. Immunofluorescence staining of KRT19 (**B**) and COL II (**C**) ($n = 3$). (**D**) Quantification of fluorescence intensity of COL II and KRT19. Data are presented as mean ± SD ($n = 3$). $^{*}p < 0.05$. ns, no significant difference. Statistical significance was determined by one-way ANOVA with a post-hocTukey test for (**A**) and (**C**). GPNPs, PBA-modified G5-dendrimers; SOX9@GPNPs, GPNPs loaded with SOX9-expressing plasmid; SIRT1@GPNPs, GPNPs loaded with SIRT1 proteins; SIRT1/SOX9@GPNPs, GPNPs assembled sequentially with SOX9- expressing plasmid and SIRT1 protein

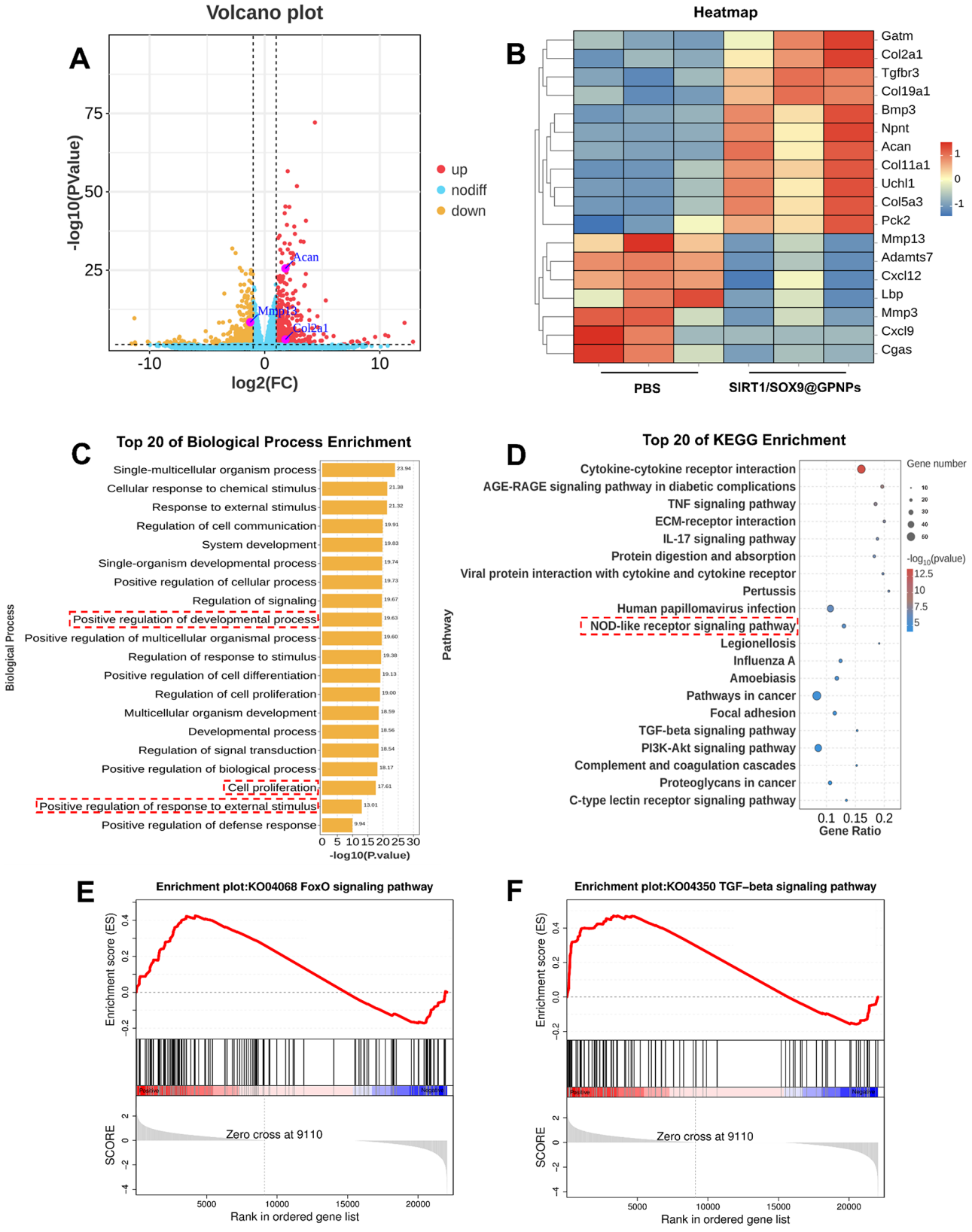

Fig. 4 Transcriptome sequencing analysis of regulatory mechanisms of multifunctional nanoplatforms. (**A**) Volcano plot showing the differential gene expression between the SIRT1/SOX9@TGPNPs group and the LPS group. (**B**) The heatmap shows the different species of DEGs between the SIRT/SOX9@TGPNPs group and the LPS group. (**C**) Top 20 of biological process enrichment bar plots. (**D**) Top 20 of KEGG enrichment analysis. GSEA of FoxO signaling pathway (**E**) and TGF-β signaling pathway (**F**). SIRT1/SOX9@GPNPs, GPNPs assembled sequentially with SOX9- expressing plasmid and SIRT1 protein

analysis (GSEA) revealed the upregulation of both FoxO and TGF-β signaling pathways. These findings further corroborate the role of the SIRT1-FoxO axis in protecting NPCs against oxidative damage, as well as the function of the SOX9-TGF-β axis in promoting ECM regeneration (Fig. 4E, F). Additionally, GSEA demonstrated that SIRT1/SOX9@GPNPs protect NPCs from various adverse factors, including "Mitophagy-animal", "Glycosaminoglycan degradation", "Apoptosis", "TNF signaling pathway", "NF-Kappa B signaling pathway", and "Chemokine signaling pathway" (Additional file 1: Figure S10).

The NOD-like receptor signaling pathway was significantly inhibited in the SIRT1/SOX9@GPNPs group (Fig. 5A). Mitochondrial dysfunction can activate the NOD-like receptor signaling pathway associated with the NLRP3 inflammasome, and the NLRP3 inflammasome cleaves procaspase-1 (Procasp-1) by combining with apoptosis-associated speck-like protein ASC [49]. The activated caspase-1 is instrumental in promoting the cleavage of GSDMD to its N-terminal fragment (GSDMD-NT), which induces cell membrane perforation and triggers pyroptosis [50]. Subsequently, we verified the inhibition of the NOD-like receptor signaling

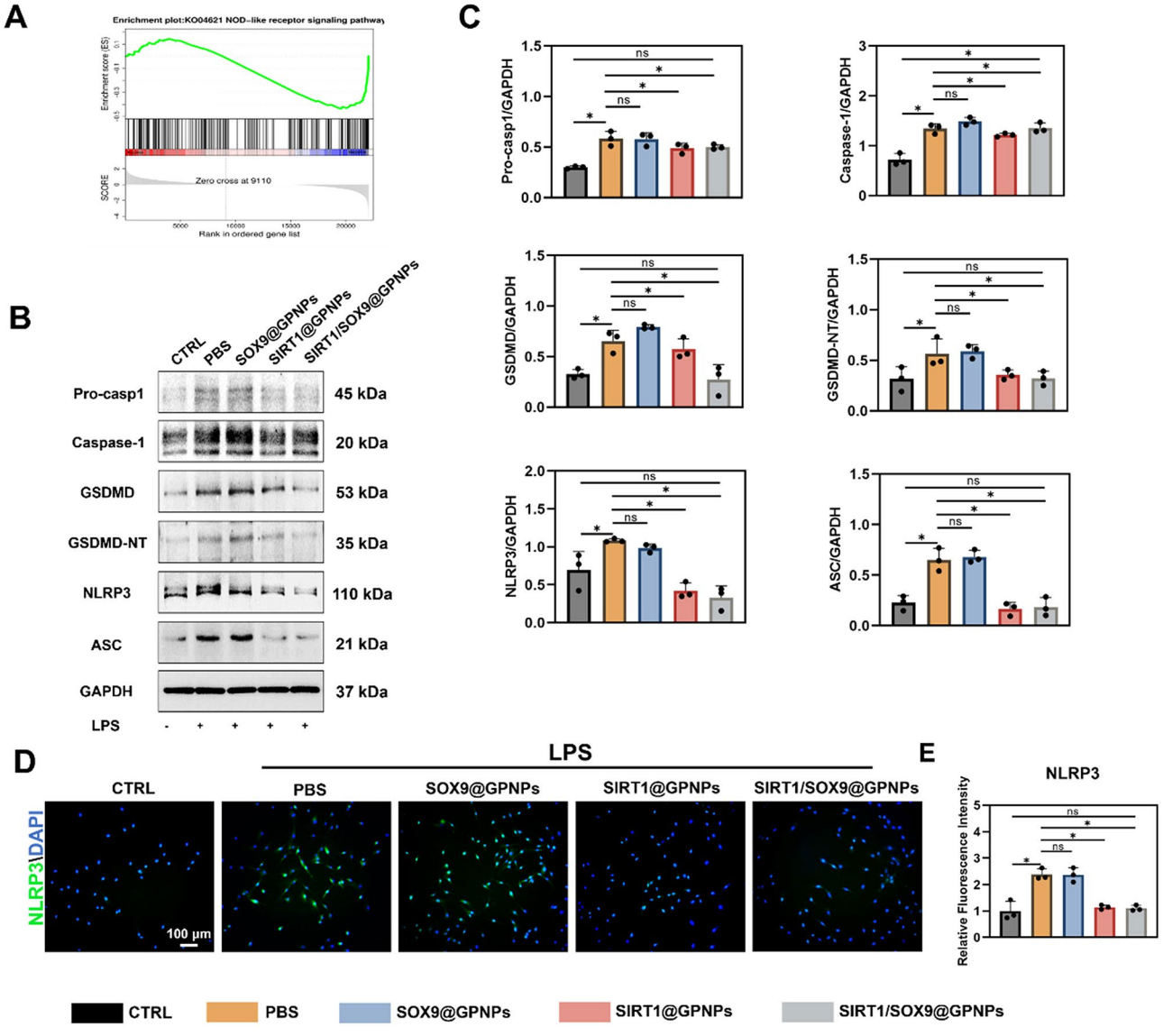

Fig. 5 Potential signaling pathways after SIRT1/SOX9@GPNPs treatment. **(A)** GSEA of NOD-like receptor signaling pathway. (**B**) Representative Western blot images of Pro-casp1, Caspase1, GSDMD, GSDMD-NT, NLRP3 and ASC protein expression in NP cells. (**C**) Quantitative analysis of the WB images ($n = 3$). (**D**) Immunofluorescence staining of NLRP3 ($n = 3$). (**E**) Quantification of fluorescence intensity of NLRP3. Data are presented as mean ± SD. $^{*}p < 0.05$. ns, no significant difference. Statistical significance was determined by one-way ANOVA with a post-hocTukey test for (**C**) and (**E**). GPNPs, PBA-modified G5-dendrimers; SOX9@GPNPs, GPNPs loaded with SOX9-expressing plasmid; SIRT1@GPNPs, GPNPs loaded with SIRT1 proteins; SIRT1/SOX9@GPNPs, GPNPs assembled sequentially with SOX9- expressing plasmid and SIRT1 protein

pathway as a mechanistic aspect of SIRT1/SOX9@GPNPs therapy through western blot experiments. We observed the upregulation of pyroptosis-related proteins after LPS induction, which did not significantly change after the intervention of SOX9@GPNPs; however, the intervention of SIRT1 and SIRT1/SOX9@GPNPs partially reversed the effect of LPS (Fig. 5B, C). Immunofluorescence further confirmed the above experimental results (Fig. 5D, E, Additional file 1: Figure S11). The cell membrane perforation induced by GSDMD-Nt can lead to a massive release of LDH into the supernatant. Compared to the control group, the SIRT1/SOX9@GPNPs group inhibited the release of LDH in the LPS-treated group, with no significant difference from the control outcomes (Additional file 1: Figure S12). These findings indicated that the repair mechanism of SIRT1/SOX9@GPNPs may involve inhibiting the NOD-like receptor signaling pathway, thereby restoring mitochondrial homeostasis and ECM balance.

Fabrication and in vitro therapeutic efficacy characterization of composite hydrogel to load the functional nanoplatform

Direct injection for IVDD often fails to maintain effective local drug concentrations for extended periods, and multiple punctures may exacerbate degeneration. To achieve stable drug concentrations in vivo, we developed a composite hydrogel system which can constantly release the functional nanoplatform. Aldehyde-functionalized hyaluronic acid was combined with gelatin methacryloyl (GelMA) and PBA-dendrimers via dynamic Schiff base linkages, and covalent bonds were introduced to enhance the hydrogel's stability. The gelation process of the hydrogel is depicted in Additional file 1: Figure S13. The microstructure of the hydrogels was examined using scanning electron microscopy (SEM). The incorporation of SIRT1/SOX9@GPNPs did not alter the porous structure of the hydrogels (Additional file 1: Figure S14). The rate of degradation of hydrogels under in vitro physiological conditions was assessed by placing them in PBS at 37 °C with a shaking rate of 100 rpm. The gradual degradation of the hydrogels as the number of days increased and the fact that hydrogels remained for more than 4 weeks (Additional file 1: Figure S15) sets the stage for the hydrogels to provide a sustained therapeutic effect. This result is reflected in the hydrogel drug release assay, where the sustained release of SOX9-expressing plasmid and SIRT1 protein from the hydrogel was maintained for more than 28 days (Additional file 1: Figure S16).

Initially, the biocompatibility of the hydrogel was tested over 1, 3, and 5 days using a CCK-8 assay. The results confirmed that NPCs proliferation in all experimental groups was unaffected compared to the control group (Additional file 1: Figure S17). NPCs were then cultured on the surfaces of hydrogels with various compositions, and assays for cell viability, adhesion, and cell spreading were performed using live/dead staining and cytoskeletal staining on days 3 and 7 (Additional file 1: Figure S18). These tests showed that SIRT1/SOX9@GPNPs@G-HA provided excellent biocompatibility.

Prior to the animal experiments, to better simulate the native microenvironment of IVDD in vivo, we induced the NPCs with LPS NPCs and cultured them in 2D and 3D, respectively. In 2D culture, cells adhere and grow on the hydrogel surface, forming a planar microenvironment. This method is operationally simple and convenient for microscope observation. However, its spatial limitations lead to differences from the in vivo environment. In 3D culture, cells are uniformly encapsulated within the hydrogel, creating a three-dimensional environment that mimics physiological conditions, making it more suitable for tissue engineering applications [32]. EDU staining is used to assess cell proliferative capacity. Then, the cells cultured on the surface of hydrogels were subjected to EDU staining and the cells cultured in hydrogels were subjected to immunofluorescence images in sections to observe whether SIRT1/SOX9@GPNPs@G-HA could maintain therapeutic effects. EDU staining showed that LPS significantly suppressed NPCs proliferation, and this phenomenon was partially reversed in SIRT1@GPNPs and SOX9@GPNPs groups; the reverse effect, greatest in the SIRT1/SOX9@GPNPs group, showed maximal promotion (Additional file 1: Figure S19). Immunofluorescence images revealed that NPCs were evenly distributed inside the hydrogel. After LPS treatment, the fluorescence intensity of NLRP3 significantly increased and the fluorescence intensity of COL II and KRT-19 decreased, while all of them were reversed in the SIRT1/SOX9@GPNPs@G-HA group (Fig. 6A). This suggested that, in the SIRT1/SOX9@GPNPs@G-HA group, LPS-induced NPCs maintained ECM secretion and phenotypic stability with the inhibited NLRP3 inflammasome expression. Then, to select the optimal concentration for animal experiments, the concentration of SIRT1/SOX9@GPNPs in the hydrogel was increased to two or three times. The doubled concentration group notably enhanced the therapeutic effects, but the tripled group resulted in significant toxicity, as evidenced by a sharp decrease in cell numbers in the hydrogel sections. Hence, a twofold concentration of SIRT1/SOX9@GPNPs@G-HA was used for animal experiments to balance efficacy and in vivo toxicity (Fig. 6A, B).

Finally, to assess in vivo release capabilities, SIRT1/SOX9@GPNPs-cy3 and SIRT1/SOX9@GPNPs-cy3@G-HA were injected into IVD for real-time fluorescence imaging. The fluorescence intensity of the SIRT1/SOX9@GPNPs-cy3 group significantly decreased by day 7, while the SIRT1/SOX9@GPNPs-cy3@G-HA group maintained a clear fluorescence intensity up to day 14. These results

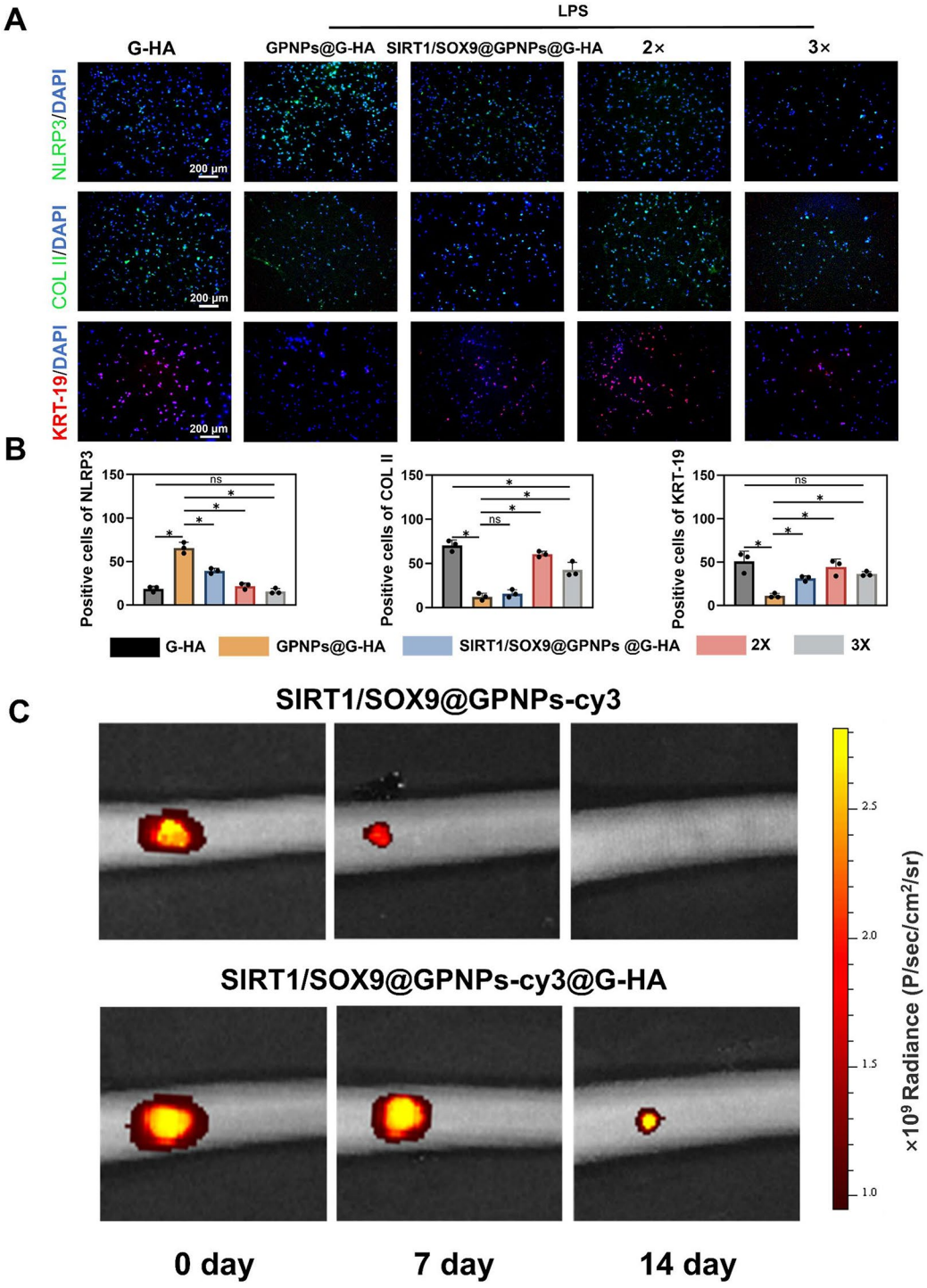

Fig. 6 Therapeutic efficacy and sustained release of composite hydrogels. (**A**) Immunofluorescence staining for NLRP3, COL II, and KRT-19 images of frozen sections of hydrogels ($n = 3$). (**B**) Quantitative analysis of fluorescence intensity of NLRP3, COL II, and KRT-19. (**C**) Representative IVIS images of rat disc at 0, 7, and 14 days. The color bar (from black to yellow) indicates the change in fluorescence signal intensity from low to high. Data are presented as mean ± SD. $^{*}p < 0.05$. ns, no significant difference. Statistical significance was determined by one-way ANOVA with a post-hocTukey test for (**B**). G-HA, hydrogel formed by crosslinking GelMA and OHA; GPNPs@G-HA, composite hydrogel loaded with GPNPs; SIRT1/SOX9@GPNPs@G-HA, composite hydrogel loaded with SIRT1/SOX9@GPNPs; 2×, composite hydrogel with double concentration of SIRT1/SOX9@GPNPs; 3×, composite hydrogel with triple concentration of SIRT1/SOX9@GPNPs; SIRT1/SOX9@GPNPs-cy3, cy3-labeled SIRT1/SOX9@GPNPs; SIRT1/SOX9@GPNPs-cy3@G-HA, composite hydrogel loaded with cy3-labeled SIRT1/SOX9@GPNPs

suggest a better retention efficiency of SIRT1/SOX9@GPNPs@G-HA in vivo (Fig. 6C).

In vivo therapeutic evaluation of the composite hydrogel loaded with the functional nanoplatform

To further assess the therapeutic efficacy of SIRT1/SOX9@GPNPs@G-HA in vivo, we established an IVDD model in Sprague Dawley rats using tail IVD puncture. Percutaneous needle puncture injury has been demonstrated as a reliable method for stably inducing an IVDD model in Sprague Dawley rat tail vertebrae [51]. The acupuncture could decrease T2-weight intensity in MRI images and induce significant histological impairment. Specifically, following damage to AF integrity, the NP tissue prolapsed during exercise, resulting in histological changes in IVD and symptoms of nerve root compression [19, 48]. We divided the rats into four groups: Sham (non-punctured) group, Defect (punctured with PBS injection) group, G-HA (punctured with G-HA injection) group, and SIRT1/SOX9@GPNPs@G-HA (punctured with SIRT1/SOX9@GPNPs@G-HA injection) group. Radiographic imaging examinations were conducted at postoperative weeks 4 and 8, and tissue samples were collected at the corresponding time points for subsequent analysis.

The DHI, quantified to measure disc height, serves as an indicator to monitor degenerative changes and therapeutic effects in IVDD (Additional file 1: Figure S20). Post-puncture, a significant decline in DHI was observed in the defect group at both postoperative weeks 4 and 8, indicating disc collapse. This decline was not alleviated in the G-HA group; however, in the SIRT1/SOX9@GPNPs@G-HA group, DHI changes were minimal, indicating a slower rate of disc collapse (Fig. 7A, C). The matrix components of NP tissue composed of collagen and glycosaminoglycans are rich in water, which is reflected in the T2-weighted signal in MRI images. Healthy NP tissue contains more matrix components to retain water, thereby maintaining normal disc function and structure, which appears as high signal intensity (white signal) on T2-weighted images. In contrast, as discs degenerate, the matrix and water content in NP tissue decrease, leading to reduced signal intensity in T2-weighted images, presenting as gray or black signals. Thus, the T2-weighted signal intensity has been widely used in the diagnosis and grading of IVDD. According to MRI images, the defect group displayed the lowest signal intensity at postoperative weeks 4 and 8, consistent with the DHI results. Among the treatment groups, the SIRT1/SOX9@GPNPs@G-HA group showed the greatest retention of water content in the nucleus pulposus, with no significant difference from the sham group (Fig. 7A, D).

We collected samples at postoperative weeks 4 and 8 for histological evaluation of disc tissue and structure integrity. As shown by H&E and SO/FG staining, non-punctured discs exhibited normal tissue and structure, with a well-preserved and well-formed nucleus pulposus. At postoperative weeks 4 and 8, puncture-induced extensive loss of nucleus pulposus tissue, severe fibrosis, and disorganized disc structures were observed. The therapeutic effect in the G-HA group was significantly limited. Notably, in the SIRT1/SOX9@GPNPs@G-HA group, most of the nucleus pulposus was preserved with the structure similar to the sham group, and the boundary between the nucleus pulposus and annulus fibrosus was clearly defined (Fig. 7B, E). Immunofluorescence staining results showed that puncture treatment significantly reduced the expression levels of COL II and ACAN, while significantly increasing MMP13 and NLRP3 expression (Fig. 8A, B). These changes indicate that puncture-induced imbalance between ECM synthesis and catabolism, and enhanced pyroptosis. Compared to the defect group, the SIRT1/SOX9@GPNPs@G-HA treatment reversed these abnormalities. SIRT1/SOX9@GPNPs@G-HA treatment not only restored the expression levels of COL II and ACAN and inhibited the overexpression of MMP13, but also significantly reduced NLRP3 expression. This suggests that the treatment restored the balance between ECM synthesis and degradation and suppressed pyroptosis, which was consistent with our in vitro results.

Lastly, in vivo application necessitates ensuring the biosafety of biomaterials to avoid adverse reactions. Therefore, we assessed the in vivo toxicity reactions across different groups during the treatment period. Four weeks after locally injecting various hydrogel components into the rat tail IVDs, we evaluated the functions of the heart, liver, spleen, lungs, and kidneys from different groups. Histological examination of major organs through H&E staining revealed no pathological changes, confirming the excellent in vivo biocompatibility of SIRT1/SOX9@GPNPs@G-HA (Additional file 1: Figure S21).

Discussion

Current research trends indicate a growing inclination toward the synergistic interventions of multiple adverse factors for IVDD. This strategy stems from a deepened understanding of the pathological mechanism of IVDD—it is not dominated by a single factor, but results from complex interactions of multiple adverse factors [52]. Therefore, it is particularly important to develop therapeutic strategies that counteract multiple unfavorable factors.

It has become clear that ROS levels play a dual role in IVDD, acting both as detrimental and beneficial agents [7]. The dynamic balance of ROS is involved in various

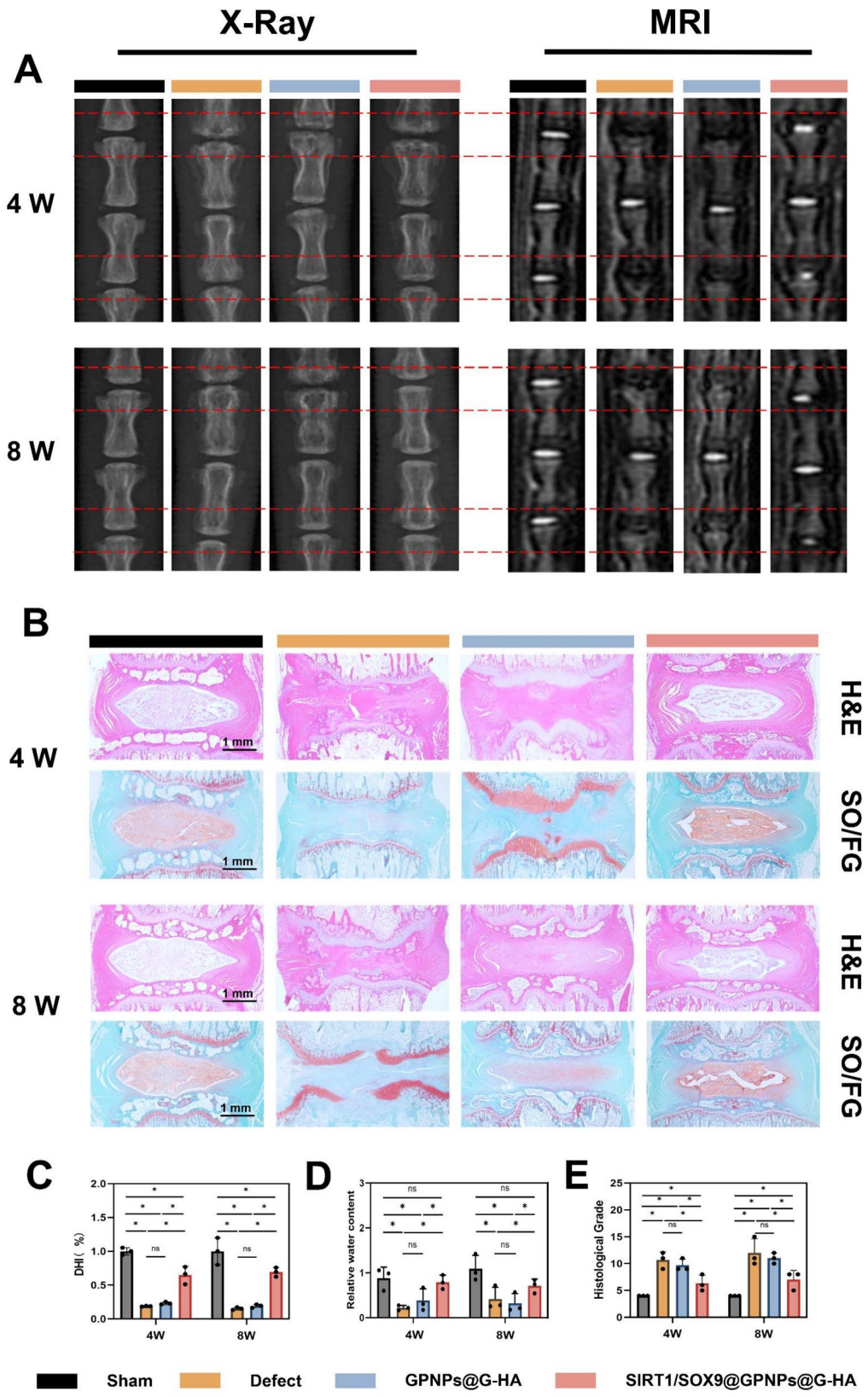

Fig. 7 (See legend on next page.)

(See figure on previous page.)

Fig. 7 In vivo therapeutic effects of composite hydrogels assessed by imaging and histology. (**A**) Representative X-Ray images and MRI images of rat tails from the Sham (non-punctured) group, Defect (punctured with PBS injection) group, G-HA (punctured with G-HA injection) group, and SIRT1/SOX9@GPNPs@G-HA (punctured with SIRT1/SOX9@GPNPs@G-HA injection) group, respectively. (**B**) H&E and SO/FG staining of the IVD after different treatments at post-operation weeks 4 and 8. Disc height index (DHI) (%) ($n = 3$) (**C**) and mean gray value ($n = 3$) (**D**) of the IVD. (**E**) Histological grade of sections in different groups at post-operation 4 weeks and 8 weeks ($n = 3$). Data are presented as mean ± SD. $^{*}p < 0.05$. ns, no significant difference. Statistical significance was determined by one-way ANOVA with a post-hocTukey test for (**C**), (**D**) and (**E**). G-HA, hydrogel formed by crosslinking GelMA and OHA; GPNPs@G-HA, composite hydrogel loaded with GPNPs; SIRT1/SOX9@GPNPs@G-HA, composite hydrogel loaded with SIRT1/SOX9@GPNPs

cellular defence regulatory mechanisms [53]. However, when this balance is disrupted by adverse factors such as aging, inflammation, or mechanical stress, the apoptosis of NPCs is triggered by the excessive accumulation of ROS [42]. If the negative impact of excessive ROS is not cleared in time, the self-repair mechanisms of NPCs or the exogenous positive repair forces may be blocked, leading to the failure of some therapeutic systems to achieve their expected outcomes. In our study, we underscored the importance of prioritizing the removal of adverse factors; directly delivered proteins can rapidly enter cells and exert immediate effects, typically reaching the intracellular environment and exhibiting biological function within 6 h. This rapid-onset characteristic makes protein delivery particularly suitable for priority interventions, such as quick clearance of harmful factors or activation of immediate protective mechanisms [54]. We reveal that a portion of SIRT1 can enter the cell nucleus, potentially regulating multiple transcription factors through deacetylation, thereby achieving enhanced therapeutic effects. This regulatory mechanism may be comprehensive and involve multiple interconnected signaling pathways, which effectively improve the microenvironment of IVD. This is consistent with the goals we aimed to achieve. SIRT1 is a protein that shuttles between the cytoplasm and nucleus [55]. Although SIRT1 is recognized for its nuclear localization sequence, the direct nuclear delivery capability of GPNPs might accelerate the nuclear entry process of SIRT1.

Existing studies achieve multidimensional interventions through the delivery of drugs or bioactive factors, but such systems lack effective correlation. In vivo biological processes are an interacting network, and systems with synergistic effects have the advantage of enhancing therapeutic outcomes [56, 57]. SOX9, as an essential transcription factor, can assist SIRT1 in enhancing the biosynthesis and maintenance of ECM [58]. Therefore, considering the complex challenges of disc degeneration, SIRT1 acts as a potent regulator capable of mitigating the negative cellular effects of the disordered microenvironment. Simultaneously, SOX9 activates the inherent regenerative capacity of the tissue, resulting in a positive reparative effect. The synergistic therapeutic approach of SIRT1 and SOX9 is essential for disc degeneration. In our study, we successfully loaded SIRT1 protein and SOX9 plasmid onto the surface of GPNPs, and delivered them intracellularly. Specifically, in in vitro experiments, we observed varying degrees of increased secretion of COL II and ACAN and maintenance of phenotype in both the SIRT1@GPNPs and SOX9@GPNPs groups, accompanied by a reduction in MMP13. The SIRT1/SOX9@GPNPs group exhibited the most significant effects, suggesting that the actions of SIRT1 and SOX9 are complementary in promoting ECM secretion and phenotype maintenance.

RNA sequencing results further prove that SIRT1 plays a central role through its deacetylation function, not only directly influencing multiple biological processes, but also synergizing with the SOX9-expressing plasmid. GSEA reveals significant enhancement of the FoxO signaling pathway and TGF-β signaling pathway, both crucial for promoting IVD repair [59, 60]. Conversely, pathways detrimental to cells, such as glycosaminoglycan degradation and inflammation-related pathways, are suppressed [61, 62]. This aligns with the ability of SIRT1 to inhibit inflammation pathways and the expression of inflammatory factors through deacetylation [63, 64]. We observed an enhancement in mitophagy, suggesting that SIRT1 may maintain mitochondrial homeostasis by regulating the mitochondrial quality control system, further highlighting its multifaceted role in cellular protection. Notably, KEGG pathway enrichment analysis indicated a marked inhibition of the NOD-like receptor signaling pathway. The NOD-like receptor signaling pathway, comprising pattern recognition receptors, is a key component of the immune system. Specifically, NLRP3 recognizes pathogen-associated molecular patterns and damage-associated molecular patterns (DAMPs), triggering immune responses and inflammation [65]. Our experiments showed reduced expression of pyroptosis-related proteins in the SIRT1/SOX9@GPNPs group. In summary, SIRT1/SOX9@GPNPs demonstrate their multifunctionality, effectively countering the negative effects of adverse factors, while actively mobilizing the intrinsic positive repair mechanisms within cells, highlighting strong therapeutic potential.

A three-dimensional network of hydrogel enables the persistent and controlled release of bioactive factors. Liu et al. developed an injectable hydrogel that responds to the pathological microenvironment of IVDD for the controlled release of anti-inflammatory drugs [66]. Seung et al. prepared an injectable hydrogel for the sustained release of DFO-NP nanochelators to treat patients with iron overload [67]. Given the excellent therapeutic effects

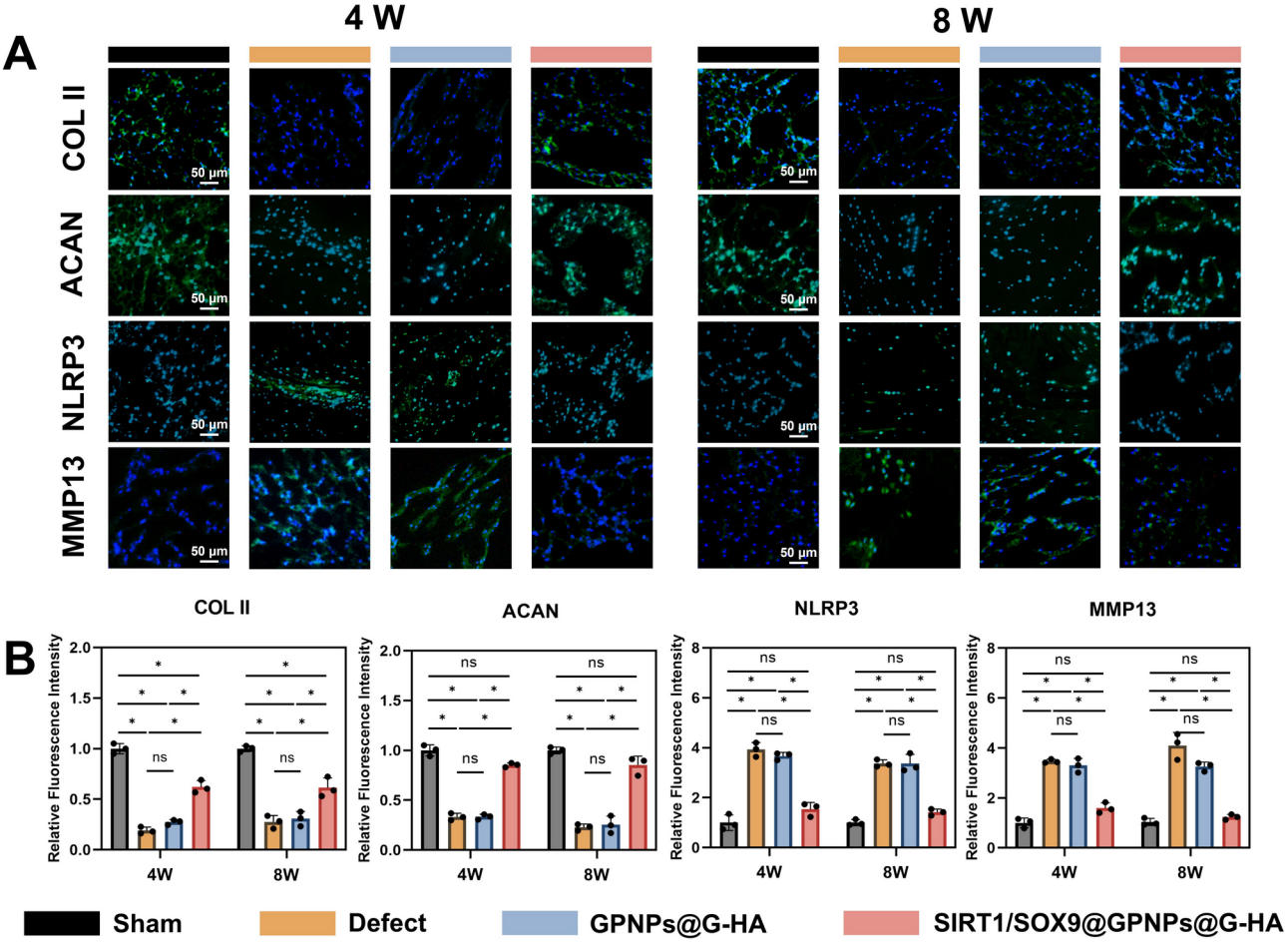

Fig. 8 SIRT1/SOX9@GPNPs@G-HA treats IVDD by alleviating ECM metabolic disorders and suppressing inflammation. (**A**) Immunofluorescence staining for COL II, ACAN, NLRP3, and MMP13 images of the rat sections ($n=3$). (**B**) Quantification analysis of fluorescence intensity of COL II, ACAN, NLRP3, and MMP13. Data are presented as mean ± SD ($n=3$). $^{*}p<0.05$. ns, no significant difference. Statistical significance was determined by one-way ANOVA with a post-hocTukey test for (**D**). G-HA, hydrogel formed by crosslinking GelMA and OHA; GPNPs@G-HA, composite hydrogel loaded with GPNPs; SIRT1/SOX9@GPNPs@G-HA, composite hydrogel loaded with SIRT1/SOX9@GPNPs

of these hydrogel systems with sustained drug release, our study employed a crosslinked network composed of GelMA and OHA for the continuous release of GPNPs. Gelatin and hyaluronic acid, derivatives from the ECM, not only create a near-natural environment for cell growth and provide the required adhesion sites, but also act as "dams" for the gradual release of drugs through their rich polymer networks and crosslinking sites [68–70]. However, the significant differences between the in vitro cell co-culture models and the in vivo microenvironment of natural cell growth might limit the therapeutic effects in vivo [71]. Therefore, before applying the hydrogel in animal experiments, it is advantageous to use 2D and 3D cell culture systems to simulate the in vivo microenvironment, compared to co-culture systems. NPCs were seeded on the surface of hydrogel or encapsulated within the hydrogel, and the SIRT1/SOX9@GPNPs@G-HA group demonstrated high cell viability and proliferation. Furthermore, its ability to inhibit NLRP3 expression, promote ECM component secretion, and maintain a stable phenotype was maintained.

The IVD is a complex fibrocartilaginous tissue between continuous vertebrae that plays a pivotal role in preserving the stability and flexibility of the spine [72]. Among the various indicators used to assess the progression of IVDD, the decrease in disc height leads to reduced mechanical stability between vertebrae and uneven force distribution. Additionally, the reduction in nucleus pulposus water content is an early sign of disc degeneration. As the water content decreases, the nucleus pulposus loses its original elasticity and buffering capacity. Our study demonstrated that, through X-Ray and MRI assessments, the SIRT1/SOX9@GPNPs@G-HA group exhibited the best therapeutic outcomes. Furthermore, following H&E and Safranin O-Fast Green staining, tissue sections observed at weeks 4 and 8 showed that the disc structure and nucleus pulposus tissue were best preserved in the SIRT1/SOX9@GPNPs@G-HA group.

Finally, immunofluorescence staining of the tissue sections was consistent with in vitro experiments, revealing that the SIRT1/SOX9@GPNPs@G-HA group expressed higher levels of COL II and ACAN, and lower levels of NLRP3 and MMP13. Generally, Direct injection of highly concentrated nanoparticles may induce toxic injuries. Therefore, in our research, hydrogels are utilized for their ability to achieve sustained release and protect tissues, thereby lessening harm to the body. In the in vivo toxicity assays, compared with the control group, the structures of major organs (heart, liver, spleen, lungs, and kidneys) in the experimental group exhibited no significant differences. This suggests that our functional composite hydrogels not only delivers effective treatment but also helps avert bodily toxicity, which is of great significance for prolonged IVDD therapy.

In summary, composite hydrogels have favourable therapeutic effects in vivo and in vitro. Compared to current IVDD therapies, such as NSAIDs that mainly target symptom relief but have limited efficacy, and biologic therapies (like growth factor injections) that have the limitation of single action [73]. In contrast, by co-loading SIRT1 protein and SOX9-expressing plasmid, the present nanoplatform inhibits multiple unfavourable factors in IVDD through sequential and synergistic treatment of SIRT1 and SOX9 on the one hand, and constructs a dynamic hydrogel using natural materials with low immunogenicity to help the sustained release of therapeutic factors on the other hand. And the multiplicity of effects and good biocompatibility make it have a stronger potential for clinical translational applications. However, based on the current research findings, several issues still need to be explored. Firstly, the NOD-like receptor signaling pathway involves multiple upstream and downstream signaling molecules and effectors, forming a complex signaling network. The molecular mechanisms of these interactions need deeper exploration. Secondly, the actual growth microenvironment of NPCs in vivo is complex and variable, influenced by hypoxia and continuous mechanical stimulation, making it unique and different from other tissue cells. Therefore, more consideration is needed regarding the structure and composition of the hydrogel to further explore an ideal candidate culture system that closely simulates the real growth microenvironment. Finally, the biomechanical evaluation of the IVD is an important indicators reflecting disc function and structure. In vivo experiments should include comparisons of the biomechanical evaluation of the disc before and after treatment to comprehensively assess the progression of degeneration. Thus, in subsequent studies, the above questions should be further tested and discussed. These future studies will enhance our understanding and application of this therapeutic strategy, potentially leading to more effective treatments for IVDD.

Conclusion

We proposed a nanoassembly strategy for the functional platform loaded with SIRT1 protein and SOX9-expressing plasmid for the intervention of multiple adverse factors, encapsulated within a hydrogel for sustained in vivo therapy. The protein and plasmid exert their effects in a time-sequential manner. GPNPs delivered SIRT1 protein and SOX9-expressing plasmid into the NPCs to balance mitochondrial homeostasis, inhibit cell apoptosis, and improve matrix metabolism while maintaining the phenotype. RNA sequencing data suggest that the therapeutic effect of SIRT1/SOX9@GPNPs may be related to the NOD-like receptor signaling pathway. To further enhance the in vivo therapeutic capability of SIRT1/SOX9@GPNPs, GPNPs were encapsulated within a G-HA hydrogel via Schiff base bonds. This hydrogel was found to release SIRT1/SOX9@GPNPs in a sustained manner in vivo, treating disc degeneration by improving matrix metabolism and suppressing excessive NLRP3 expression. Overall, this study presents an effective therapeutic strategy for the intervention and repair of IVDD, showing significant potential for application.

Materials and methods

Materials

Amine-terminated G5 PAMAM was purchased from Weihai Chenyuan Molecular New Material Co., Ltd. (Shandong, China). 4-(Bromomethyl)phenylboronic acid (PBA), gelatin, N-hydroxysuccinimide (NHS), $NaIO_4$, and ethylene glycol were purchased from Aladdin (Shanghai, China). GelMA (EFL-GM-60) and lithium pheny1-2,4,6-trimethybenzoylphosphinate (LAP) were purchased from Suzhou Intelligent Manufacturing Research Institute (Suzhou, China). Dulbecco's modified Eagle's medium, Ham's F-12 medium (DMEM/F12), and fetal bovine serum (FBS) were purchased from Gibco (Carlsbad, CA).

Synthesis and characterization of G5-PBA-dendrimer nanoplatforms (GPNPs)

As mentioned previously, PBA-functionalized dendritic macromolecules were synthesized via the following method, in which phenylboronic acid (PBA) was grafted onto the surface of dendritic macromolecules through a substitution reaction under heating conditions [37]. First, amine-terminated G5 dendritic macromolecules and 4-(bromomethyl)phenylboronic acid were dissolved in a 40 mL anhydrous methanol beaker at a molar ratio of 1:256, followed by thorough stirring at 70 °C for 24 h. The reaction product was transferred into a dialysis bag (MWCO = 3500 Da) and extensively dialyzed against anhydrous methanol and deionized water to remove

unreacted substances, impurities, and solvents, with the dialysis solution replaced every 3 h. The purified product was freeze-dried to obtain para-PBA-modified dendritic macromolecules. The fully purified product was characterized using 1 H nuclear magnetic resonance (1 H NMR) spectroscopy, and the average number of PBA molecules grafted per dendritic macromolecule was calculated based on the integral areas corresponding to the characteristic peaks of PBA and the dendritic macromolecules.

Preparation of SOX9@GPNPs, SIRT1@GPNPs, and SOX9/SIRT1@GPNPs

The preparation of SOX9@GPNPs, SIRT1@GPNPs, and SOX9/SIRT1@GPNPs was conducted separately. For SOX9@GPNPs preparation, GPNPs were mixed with SOX9 expression plasmid (0.8 μg) at N/P ratios (0, 1, 2, 4, 8, 16) in 100 μl solution according to a previously reported method for N/P ratio calculation [37]. The corresponding GPNP masses were 0, 0.18 μg, 0.36 μg, 0.72 μg, 1.44 μg, and 2.88 μg. The mixtures were vortexed thoroughly for 3 min and incubated at 25 °C for 30 min. For agarose gel electrophoresis, samples with different N/P ratios and DNA marker were loaded onto a 1% agarose gel. Electrophoresis was performed in 1×TAE buffer at 130 V for 30 min, and band patterns were visualized using a gel imaging system. Subsequently, SOX9@GPNPs were diluted with PBS to 1 ml for hydrodynamic size and zeta potential measurements using a Zetasizer Nano-ZS (Malvern, UK) at room temperature. Parameters including size distribution, average particle size, and PDI were recorded. For SIRT1@GPNPs preparation, SIRT1 protein was mixed with GPNPs at W/W ratios (0, 2, 4, 8) in 100 μl solution, corresponding to SIRT1 masses of 0, 2.88 μg, 5.76 μg, and 11.52 μg (with fixed GPNP mass of 1.44 μg based on the optimal N/P ratio for SOX9@GPNPs). The mixtures were vortexed for 3 min, incubated at 25 °C for 30 min, and then diluted to 1 ml with PBS for hydrodynamic size and zeta potential measurements using the same protocol as SOX9@GPNPs. For SOX9/SIRT1@GPNPs preparation, SOX9 plasmid (0.8 μg) was first complexed with GPNPs (1.44 μg) at N/P = 8, followed by the addition of SIRT1 protein (2.88 μg). Other steps followed the protocols for SOX9@GPNPs and SIRT1@GPNPs. The final complexes were diluted to 1 ml with PBS for hydrodynamic size analysis. The particle size stability of GPNPs, SOX9@GPNPs, and SIRT1/SOX9@GPNPs was monitored at 0, 12, 24, and 36 h during PBS storage. Additionally, the morphology of SIRT1/SOX9@GPNPs was characterized by TEM (JEOL JEM 2100 F).

Intracellular delivery of nanocomplexes

The prepared SOX9@GPNPs, SIRT1@GPNPs, and SOX9/SIRT1@GPNPs were diluted to 500 μl using DMEM/F12 complete medium containing 10% fetal bovine serum (FBS) and 1% penicillin/streptomycin for subsequent cell culture and incubated in a 37 °C, 5% CO_2 humidified incubator. For cytotoxicity testing, NPCs were seeded into 96-well plates to ensure uniform distribution. Groups included SOX9@GPNPs at varying N/P ratios (0, 1, 2, 4, 8, 16) and SIRT1@GPNPs at varying W/W ratios (0, 2, 4, 8). The complexes were added to designated wells and cultured for 24 h. After incubation, 100 μL CCK-8 reagent (dissolved in sterile DMEM/F12 medium, Beyotime, China) was added to each well and incubated in the dark for 1 h. Absorbance at 450 nm was measured using a full-wavelength microplate reader. To evaluate GPNPs' plasmid DNA delivery efficiency, GPNPs were mixed with pcDNA3.1-Sox9-ZsGreen1 at N/P ratios of 0, 1, 2, 4, 8, and 16. When NPCs reached 80% confluency, the mixtures were added to the culture medium. After 6 h incubation, the medium was replaced, and cells were cultured for an additional 18 h. Green fluorescence expression was observed under an inverted microscope. Successful delivery by SOX9@GPNPs was confirmed by detecting *Sox9*, *Col2a1* and *Acan* gene expression (NC group: *Sox9* none-expressed; SOX9@GPNPs: *Sox9* expressed). Total RNA was extracted using TRIzol reagent (Invitrogen, American), quantified with NanoDrop 2000 spectrophotometers (Thermo Fisher Scientific, American), reverse-transcribed into cDNA, and amplified following manufacturer protocols. Primer sequences (Sangon Biotech, Shanghai, China) are detailed in Table S1. Gene expression levels were normalized to GAPDH. For protein delivery assessment, BSA-FITC (green fluorescent) was used as a model protein. Groups included control, GPNPs, BSA-FITC, and BSA-FITC@GPNPs (WBSA-FITC: WGPNPs = 1.5:1; 2.16 μg BSA-FITC, 1.44 μg GPNPs). After 6 h treatment, NPCs were fixed with 4% paraformaldehyde, stained for cytoskeleton (37 °C, dark, 1 h), and nuclei (DAPI). Fluorescence distribution was observed under an inverted microscope. To evaluate intracellular ROS levels before and after SIRT1 delivery, a DCFH-DA probe-based fluorescence assay was performed. Groups included CTRL (Control no other treatment), PBS/LPS (PBS and LPS co-treatment), FREE SIRT1/LPS (SIRT1 protein and LPS co-treatment), and SIRT1@GPNPs/LPS (SIRT1@GPNPs and LPS co-treatment). The concentration of LPS was 1 μg/mL. NPCs were seeded in 24-well plates, cultured to 80–90% confluency in DMEM/F12 medium, and treated according to groups for 24 h. After washing with serum-free medium, DCFH-DA working solution (1:1000 dilution in PBS, Beyotime, China) was added and incubated (37 °C, dark, 20 min). Nuclei were stained with Hoechst 33,342 (Beyotime, China) for 10 min. Fluorescence was observed under a fluorescence microscope. Sequential delivery was monitored by delivering BSA-FITC and pcDNA3.1-Sox9-DsRed plasmid (2.16 μg BSA-FITC,

1.44 μg GPNPs, 0.8 μg plasmid) into cells. Fluorescence distribution was observed at 6, 12, 24, and 48 h post-delivery. For follow-up experiments (antioxidant, mitochondrial function, ECM synthesis/catabolism, and phenotypic assays), groups included: (1) Normal medium (CTRL); (2) PBS + 1 μg/mL LPS (PBS group); (3) SOX9@GPNPs + 1 μg/mL LPS (SOX9@GPNPs group); (4) SIRT1@GPNPs + 1 μg/mL LPS (SIRT1@GPNPs group); (5) SIRT1/SOX9@GPNPs + 1 μg/mL LPS (SIRT1/SOX9@GPNPs group). NPCs were seeded in 24-well plates, treated with group-specific solutions for 6 h after reaching 80% confluency, washed twice to remove residual medium, and incubated in fresh complete medium post-treatment.

Extraction and culture of NPCs

NPCs were isolated from the tail vertebrae of 6-week-old male Sprague–Dawley rats. Under sterile conditions, the nucleus pulposus tissue was removed from the IVDs and incubated at 37 °C for 4 h in a 0.25% type II collagenase solution (Yuanye, Shanghai, China). Following incubation, the digested mixture was collected, centrifuged to separate the cells, and the supernatant was discarded. The resulting cell pellet was then resuspended in DMEM/F12 medium enriched with 10% FBS. Once the cells had attached, the culture medium was refreshed every two days, and cell morphology was routinely inspected.

Biocompatibility evaluation of SOX9@GPNPs and SIRT1@GPNPs

The in vitro cytotoxicity was assessed using the CCK8 assay. Approximately 6,000 cells were seeded in a 96-well plate and incubated overnight for attachment. Grouping was based on the aforementioned culture systems, and each group had three replicates. The next day, NPCs were treated with different formulations for 24 h and then incubated with 100 μl CCK8 solution for an additional 1 h. Absorbance at 450 nm was measured using a spectrophotometer (Invitrogen, USA).

Mitochondrial membrane potential detection

The mitochondrial membrane potential was assessed using the JC-1 dye, a sensitive indicator for mitochondrial membrane potential, as per the manufacturer's instructions (Beyotime, China). The functional mechanism of JC-1 relies on its aggregation state in response to the membrane potential: it forms red fluorescent J-aggregates at high potentials and exists as green fluorescent monomers at low potentials. Prior to staining, NPCs were washed with PBS, then treated with pre-warmed JC-1 dye (1:200) and the nuclear stain Hoechst 33,342, respectively, at 37 °C for 30 min. Following staining, cells were washed three times with PBS to remove unbound dye. Finally, the stained cells were visualized under an inverted microscope to assess the intensity and distribution of red and green fluorescence, and fluorescence intensity was analyzed using ImageJ software.

MitoSOX red detection

To measure mitochondrial ROS (mtROS), we employed MitoSOX Red, a fluorescent probe specifically designed to detect superoxide in mitochondria (MCE), following the manufacturer's protocol. For staining, a working solution of MitoSOX Red at 10 μM was prepared. Following the removal of the culture medium, a freshly prepared MitoSOX Red working solution was added to cover all cells. The cells were subsequently incubated in darkness at 37 °C and 5% CO2 for 30 min, and then stained with Hoechst 33,342 under the same environmental conditions. After the incubation period, the cells were carefully washed three times with PBS to eliminate any unbound dye. The cells were then examined using an inverted microscope, and the analysis was performed using ImageJ software.

Microscopic observation of mitochondria by TEM

For the microscopic observation of mitochondria by transmission electron microscopy (TEM) (JEOL JEM F200,Japan), NPCs were collected after stimulation and centrifuged. The culture medium was discarded, and the cells were fixed with pre-cooled electron microscopy fixative at room temperature for 2 h. The cell pellet was then processed further: it was washed three times with 0.1 M phosphate buffer (pH 7.2), refixed with 1% osmium tetroxide, and washed again three times with the same phosphate buffer. Afterward, the samples underwent dehydration in a graded series of alcohols, infiltration, and embedding in resin. The resin blocks were sliced into ultrathin Sect. (50 nm) for staining. Ultimately, the sections were observed under a transmission electron microscope.

Flow detection

The collected cells were resuspended in PBS and centrifuged at 300 g for 5 min. After discarding the supernatant, the cells were resuspended in binding buffer and adjusted to a concentration of 1×10^6 cells/ml. Annexin-V/PI staining was conducted in darkness. Flow cytometry analysis was performed using a flow cytometer (Merck Millipore, Germany). Subsequently, FlowJo software was utilized to determine the proportions of cells in different states and to calculate the apoptosis rate for each group.

Western blot

Proteins were extracted from NPCs under various conditions using RIPA buffer with protease inhibitors (Thermo Fisher, USA). Protein concentration was measured with a BCA Assay Kit (Beyotime, China). After denaturing the

proteins at temperatures exceeding 95 °C, equal volumes were loaded onto a 10% SDS-PAGE gel for electrophoresis. Proteins were then transferred to a PVDF membrane (Millipore, USA). The membrane was blocked for 2 h and incubated with a diluted primary antibody (1:1,000) at 4 °C overnight. The next day, the membrane was washed with TBST, incubated with a diluted secondary antibody (1:1,000) for 2 h, and washed again. The membrane was scanned, and band intensity was analyzed using ImageJ to assess protein expression. Antibodies used are listed in Table S2.

Immunofluorescence staining

Roughly 10,000 NPCs were plated in a 24-well dish and left to adhere overnight. The next day, various stimuli were introduced. NPCs were immobilized with 4% paraformaldehyde at ambient temperature and subsequently blocked with an immunostaining solution (Beyotime, China) incorporating Triton X-100 for an hour. Cells were then incubated with diluted primary antibodies (1:200; targeting COL II, KRT-19, NLRP3, Caspase-1, GSDMD) at 4 °C overnight. The following day, after three PBST washes, cells were exposed to diluted fluorescent secondary antibodies for two hours. Observations were conducted using an inverted microscope, and fluorescence strength was analyzed quantification via imageJ software.

Alcian blue staining

Alcian Blue forms a blue insoluble complex with glycosaminoglycans, indicating positive staining under a microscope. After fixing the cell samples with 4% paraformaldehyde, they were washed three times with PBS. Alcian blue staining was then performed by adding 500 µl of Alcian staining solution. After staining, samples were thoroughly washed with PBS to remove unbound dye. Finally, the staining results were observed under a microscope.

RNA sequencing and differential bioinformatic analyses

To explore the impact of LPS and SIRT1/SOX9@GPNPs (SSGP) on gene expression patterns, RNA sequencing analysis was carried out. This involved two study groups: the LPS group and the SSGP group, each with three biological replicates. RNA was isolated from the treated cells with TRIzol reagent (Invitrogen, Carlsbad, CA), and its quality and integrity were evaluated. The sequencing of RNA libraries was performed on the Illumina platform by Genedenovo Biotechnology Co., Ltd (Guangzhou, China). DESeq2 was utilized for differential gene expression analysis, where genes with an adjusted p-value less than 0.05 and an absolute log2 fold change greater than 1 were considered significantly differentially expressed.

Preparation of oxidised hyaluronic acid

First, 1.5 g of hyaluronic acid was placed in a beaker, and 150 mL of deionized water was added. The mixture was stirred at room temperature using a magnetic stirrer until the hyaluronic acid was completely dissolved. Subsequently, to oxidize the hyaluronic acid, 802 mg of sodium periodate ($NaIO_4$) was added to the solution as an oxidizing agent, followed by thorough stirring for 2 h. After the reaction, 200 µL of ethylene glycol was added to terminate the process. The resulting product was transferred into a dialysis bag, sealed, and dialyzed in deionized water. The deionized water was replaced every 3 h over 48 h to thoroughly remove small-molecule impurities. After dialysis, the purified product was freeze-dried to obtain OHA. The prepared OHA sample was sealed in a 50 mL centrifuge tube and stored in a 4 °C refrigerator for subsequent experiments.

Preparation and characterization of composite hydrogels

First, the previously prepared SOX9@GPNPs, SIRT1@GPNPs, and SOX9/SIRT1@GPNPs were crosslinked with OHA, respectively, and stirred until fully dissolved. Subsequently, gelatin methacryloyl (GelMA) with a substitution degree of 60% and the photoinitiator lithium phenyl-2,4,6-trimethyl-benzoyl phosphinate (LAP) were added to the above solution for further crosslinking. After stirring until complete dissolution, the hydrogel prepolymer was obtained. The final concentrations were 5% for GelMA, 1% for OHA, and 0.05% for LAP. Each milliliter of the prepolymer contained 0.8 µg of SOX9-expressing plasmid, 1.44 µg of GPNPs, and 2.88 µg of SIRT1 protein. The precursor solution was photo-crosslinked for 1 min using a blue light source with a wavelength of 405 nm, yielding the composite hydrogels SOX9@GPNPs@G-HA, SIRT1@GPNPs@G-HA, and SOX9/SIRT1@GPNPs@G-HA. These hydrogels were then freeze-dried and stored at 4 °C. The freeze-dried samples were cut into slices approximately 2 mm thick. The dried hydrogel slices were adhered to SEM sample stubs using conductive adhesive and sputter-coated with gold using an ion sputter coater (coating parameters: 20 mA current, 45 s). Finally, the microstructures of the hydrogels were observed using scanning electron microscopy (SEM). To investigate the in vitro degradation of the hydrogels under physiological conditions, newly prepared hydrogel samples (500 µL) were incubated in PBS at 37 °C with a rotation speed of 100 rpm. The samples were weighed (Wt) on the 7th, 14th, 21st, and 28th days. Subsequently, the degradation of the hydrogels was computed using the following formula: weight remaining (%) = Wt/W0 × 100%. To test the release of SOX9-expressing plasmid and SIRT1 protein, 500 µL SIRT1/SOX9@GPNPs@G-HA hydrogel was prepared. Hydrogels were put into 2 mL PBS and then placed in a constant temperature shaker (37 °C, 80 cycles/min).

At desired time points (1 d, 3 d, 5 d, 7 d, 14 d and 28 d), the whole medium was taken out, and an equal amount of fresh medium was added. The supernatant was evaluated by nanodrop (Thermo Fisher, American) and SIRT1 ELISA (Solarbio, China).

NPCs seeding and culturing on hydrogel surfaces (2D Culture)

First, the prepared hydrogel materials underwent strict sterilization. Subsequently, 300 μL of sterilized hydrogel solution was evenly inoculated into each well of a 24-well plate and photocrosslinked for 1 min using a 405 nm blue light source. After complete hydrogel solidification, NPCs were added to the plate at a density of 2×10^4 cells/well, and the plate was gently shaken repeatedly to ensure uniform cell distribution on the hydrogel surface. After seeding, the 24-well plate was placed in a constant-temperature cell culture incubator for incubation. The experimental groups included the G-HA group, GPNPs@G-HA group, SOX9@GPNPs@G-HA group, SIRT1@GPNPs@G-HA group, and SIRT1/SOX9@GPNPs@G-HA group. For cytotoxicity testing, the CCK-8 assay was performed on days 1, 3, and 5 post-seeding according to the manufacturer's instructions. During measurement, 100 μL of CCK-8 reagent (dissolved in sterile DMEM/F12 medium) was added to each well, followed by 1 h of incubation in the dark. Finally, the absorbance of each well was measured at 450 nm using a full-wavelength microplate reader. For live/dead staining, cytotoxicity was assessed on days 3 and 5 post-seeding using the live/dead staining method as per the manufacturer's protocol. After the culture period, the medium was gently aspirated to avoid damaging the hydrogel and cells, and the wells were washed three times with PBS. Calcein AM/PI detection working solution (Beyotime, China) was then added, and the cells were incubated at 37 °C in the dark for 30 min. After three additional PBS washes, the samples were observed under a fluorescence microscope. For cytoskeleton staining, cell morphology was evaluated on days 3 and 5 post-seeding using cytoskeleton staining according to the manufacturer's instructions. After aspirating the medium and washing with PBS three times, the cells were fixed with 4% paraformaldehyde at room temperature for 40 min, washed three times with PBS, and then treated with blocking solution containing Triton-X-100 (Beyotime, China) for 30 min to enhance cell membrane permeability. Rhodamine-labeled phalloidin working solution (prepared by diluting phalloidin stock solution 1:200 with PBS, Yuanye, China) was used to stain the cytoskeleton, followed by 40 min of incubation at 37 °C in the dark. After discarding the medium and washing with PBS three times, the nuclei were labeled with DAPI (Beyotime, China) for 5 min. The cells were washed again with PBS and observed under a fluorescence microscope. For EdU staining, NPC proliferation on the hydrogel surface was assessed on day 3 post-seeding using the EdU staining method. According to the manufacturer's instructions, NPCs were stained with EdU working solution (Beyotime, China) and DAPI, followed by fluorescence microscopy observation.

NPCs encapsulation and culturing within hydrogels (3D Culture)

First, the prepared composite hydrogel materials were subjected to sterile processing. Subsequently, NPCs were digested and collected from culture dishes, then mixed with the hydrogel solution. The cell concentration was adjusted to 2×10^6 cells/mL, and the mixture was gently homogenized to avoid bubble formation or cell aggregation. The uniformly mixed cell-hydrogel suspension was dispensed at 50 μL/well, photocrosslinked for 1 min using a 405 nm blue light source, and then transferred to a 24-well plate pre-filled with complete medium. The plate was incubated in a constant-temperature cell culture incubator. During cultivation, the medium was replaced every other day to ensure nutrient sufficiency, and cell growth was monitored under an optical microscope. Subsequent experimental groups included the G-HA group, GPNPs@G-HA group, SIRT1/SOX9@GPNPs@G-HA group, 2× group (SIRT1/SOX9@GPNPs concentration doubled compared to the original hydrogel preparation, with other components unchanged), and 3× group (SIRT1/SOX9@GPNPs concentration tripled compared to the original hydrogel preparation, with other components unchanged).

Hydrogel frozen sections and Immunofluorescence staining

After 7 days of 3D culture, the cell-hydrogel composite samples were fixed in 4% paraformaldehyde. Following fixation, the samples underwent sucrose gradient dehydration, were embedded in OCT (Biosharp, China), and flash-frozen in liquid nitrogen to prepare frozen specimens. Frozen sections were then cut at a thickness of 10 μm. The sections were subjected to antigen retrieval using citrate sodium buffer (Beyotime, China) and exposed to hydrogen peroxide solution for 10 min to eliminate endogenous peroxidase activity. Subsequently, the sections were sealed with blocking agent and incubated overnight at 4 °C with diluted primary antibodies. The next day, after washing three times with PBST, fluorescent secondary antibodies were added for staining. Finally, the sections were observed under a fluorescence microscope.

In vivo release efficiency of SIRT1/SOX9@GPNPs

For Cy3 labeling of GPNPs, GPNPs were dissolved in PBS, and Cy3 (Cy3 to GPNPs molar ratio of 3:1) was

added to the solution. The mixture was reacted at room temperature under light-protected conditions for 24 h. The reaction product was transferred into a dialysis bag and thoroughly dialyzed against PBS and deionized water, with the dialysis solution replaced every 3 h over a 24-hour period. After dialysis, the product was freeze-dried, weighed, labeled as GPNPs-Cy3, and stored in a light-protected − 20 °C freezer. To investigate the in vivo release kinetics of the composite hydrogel, 10-week-old male Sprague-Dawley rats were randomly divided into two groups. One group received direct injection of SIRT1/SOX9@GPNPs-Cy3 into the caudal vertebrae, while the other group was injected with SIRT1/SOX9@GPNPs-Cy3@G-HA composite hydrogel. Fluorescence intensity changes were monitored using an IVIS imaging system at postoperative days 0, 7, and 14.

Surgical establishment of the rat model of IVDD

All procedures were carried out in accordance with the NIH Guide for the Care and Use of Laboratory Animals and approved by the Institutional Animal Care and Use Committee of Soochow University (SUDA20240415A02). Thirty adult male rats, weighing about 300 g and aged between 8 and 10 weeks, were obtained from the Experimental Animal Center at Soochow University. The rats were randomly divided into four experimental groups: Sham, Defect, G-HA, and SIRT1/SOX9@GPNPs@G-HA. The concentration of hydrogel was 2×. In the Sham group, no puncture surgery was performed. In the Defect group, puncture surgery was carried out, but no therapeutic agents were injected; only 10 μl of PBS was injected. In the G-HA group, puncture was performed and 10 μl of G-HA hydrogel was injected. Finally, in the SIRT1/SOX9@GPNPs@G-HA group, puncture was conducted and 10 μl of SIRT1/SOX9@GPNPs@G-HA hydrogel was injected. Specifically, prior to surgery, the workbench and rat coccyges were sterilized. To minimize the interference of adjacent degenerated segments, a 20-G needle was used to puncture the central NP tissue of the 7–8th (Co7–8) and 9–10th (Co9–10) coccygeal segments to a depth of 5 mm, rotated 360°, and held in place for 30 s. Then, PBS and different compositions of hydrogels were injected at the puncture sites. Post-surgery, the coccygeal area was sterilized again, and rats were transferred to a constant temperature and ventilated environment for recovery.

Radiological imaging assessment

Radiological imaging of the rats was conducted at 4 and 8 weeks post-surgery, with the animals in an anesthetized and supine state. Normalization of the DHI was achieved using X-Ray images processed via Image J software. Additionally, T2-weighted MRI scans of the intervertebral discs were acquired using a 1.5T MRI scanner (Magnetom Essenza, Siemens Medical Solution, Erlangen, Germany) and subsequently analyzed using Image J to determine white signal intensity.

Histological and Immunofluorescence assessment of in vivo therapeutic effects

At 4 and 8 weeks, coccygeal samples from the SD rats were harvested and preserved in formalin for 24 h. Following fixation, the samples underwent a 30-day decalcification process in 10% EDTA. The NP tissue was then extracted, embedded in paraffin, and sliced into 5 μm sections. These sections were subjected to H&E and Safranin O/Fast Green (SO/FG) staining techniques to visualize the disc structure and the distribution of matrix components. Subsequently, the degree of disc degeneration was evaluated and graded based on established histological grading criteria.

Supplementary Information

The online version contains supplementary material available at https://doi.org/10.1186/s12951-025-03401-2.

Supplementary Material 1

Acknowledgements

Not applicable.

Author contributions

Xiaoyu Zhang and Qianping Guo contributed equally to this work. Xiaoyu Zhang, Qianping Guo, Caihong Zhu, Bin Li and Li Ni Conceived and designed the research; Xiaoyu Zhang, Qianping Guo, Jiawei Fang, Qi Cheng, Zhuang Zhu and Qifan Yu performed the experiments; Huan Wang and Youzhi Hong provided technical support and analyzed the data; Xiaoyu Zhang, Qianping Guo and Chengyuan Liu wrote the manuscript; Huilin Yang, Caihong Zhu, Bin Li and Li Ni reviewed and revised the manuscript. All authors discussed and commented on the manuscript.

Funding

This study was supported by the National Natural Science Foundation of China (32371414, 81902248, 81925027, 32130059 and 81871805), the China Postdoctoral Science Foundation (2021M702393), the Suzhou Science and Technology Planning Project (SKY2023148), and the Priority Academic Program Development of Jiangsu Higher Education Institutions.

Data availability

Data is provided within the manuscript or supplementary information files.

Declarations

Ethics approval and consent to participate

All animal experiments in this study were approved by the Institutional Animal Care and Use Committee of Soochow University.

Consent for publication

All authors agree to be published.

Competing interests

The authors declare no competing interests.

Author details

[1]Department of Orthopedic Surgery, Medical 3D Printing Center, The First Affiliated Hospital, Orthopedic Institute, School of Basic Medical Sciences,

MOE Key Laboratory of Geriatric Diseases and Immunology, Suzhou Medical College, Soochow University, Suzhou, Jiangsu 215000, China

Received: 13 December 2024 / Accepted: 15 April 2025
Published online: 10 May 2025

References

1. GBD 2017 Disease. And injury incidence and prevalence collaborators. Lancet. 2018;392:1789–858.
2. Urits I, Capuco A, Sharma M, Kaye AD, Viswanath O, Cornett EM, Orhurhu V. Curr Pain Headache Rep. 2019;23;65.
3. Mohd Isa IL, Teoh SL, Mohd Nor NH, Mokhtar SA. Int J Mol Sci. 2023;24;208.
4. Grunhagen T, Shirazi-Adl A, Fairbank JCT, Urban JPG. Orthop Clin North Am. 2011;42:465–77.
5. Huang YC, Urban JPG, Luk KDK. Nat Rev Rheumatol. 2014;10:561–6.
6. Silagi ES, Shapiro IM, Risbud MV. Matrix Biol. 2018;10;71–72;368–379.
7. Xia Q, Zhao Y, Dong H, Mao Q, Zhu L, Xia J, Weng Z, Liao W, Hu Z, Yi J, Feng S, Jiang Y, Xin Z. Biomed Pharmacother. 2024;174;116593.
8. Wang Y, Cheng H, Wang T, Zhang K, Zhang Y, Kang X. Cell Prolif. 2023;56:e13448.
9. Lisiewski LE, Jacobsen HE, Viola DCM, Kenawy HM, Kiridly DN, Chahine NO. FASEB J. 2024;38e23364.
10. Fert-Bober J, Murray CI, Parker SJ, Van Eyk JE. Circ Res. 2018;122:1221–37.
11. Zhu D, Liang H, Du Z, Liu Q, Li G, Zhang W, Wu D, Zhou X, Song Y, Yang C. Research. 2024;7;0350.
12. Duan G, Walther D. PLoS Comput Biol. 2015;11:e1004049.
13. Lin H, Caroll KS. Chem Rev. 2018;118:887–8.
14. Pieroni S, Castelli M, Piobbico D, Ferracchiato S, Scopetti D, Di-Iacovo N, Della-Fazia MA, Servillo G. Int J Mol Sci. 2022;23;14480.
15. Lu C, Zhao H, Liu Y, Yang Z, Yao H, Liu T, Gou T, Wang L, Zhang J, Tian Y, Yang Y, Zhang H. Int J Bio Sci. 2023;19:484–501.
16. Mahlooji MA, Heshmati A, Kheirpour N, Ghasemi H, Asl SS, Solgi G, Ranjbar A, Hosseini A. Drug Res. 2021;72:100–8.
17. Yang G, Jin L, Zheng D, Tang X, Yang J, Fan L, Xie X. Mar Drugs. 2019;17;702.
18. Wu QJ, Zhang TN, Chen HH, Yu XF, Lv JL, Liu YY, Liu YS, Zheng G, Zhao JQ, Wei YF, Guo JY, Liu FH, Chang Q, Zhang YX, Liu CG, Zhao YH. Signal Transduct Target Ther. 2022;7:1–74.
19. Wang P, Yang C, Lu J, Ren Y, Goltzman D, Miao D. J Orthop Translat. 2023;40:13–26.
20. Le Maitre CL, Pockert A, Buttle DJ, Freemont AJ, Hoyland JA. Biochem Soc Trans. 2007;35:652–5.
21. Zhu Z, Yu Q, Li H, Han F, Guo Q, Sun H, Zhao H, Tu Z, Liu Z, Zhu C, Li B. Bioact Mater. 2023;28:167–82.
22. Gruber HE, Norton HJ, Ingram JA, Hanley ENJ. Spine. 2005;30;625.
23. Tsingas M, Otone OK, Haseeb A, Barve RA, Shapiro IM, Lefebvre V, Risbud MV. Matrix Biol. 2020;94:110–33.
24. Kondo M, Yamaoka K, Tanaka Y. Int J Mol Sci. 2014;15:21270–85.
25. Müller JA, Schäffler N, Kellerer T, Schwake G, Ligon TS, Rädler JO. Eur J Pharm Biopharm. 2024;197;114222.
26. Tian Y, Tirrell MV, LaBelle JL. Adv Healthc Mater. 2022;11;2102600.
27. Hong Y, Duan Y, Zhu Z, Yu Q, Mo Z, Wang H, Zhou T, Liu Z, Bai J, Zhang X, Yang H, Zhu C, Li B. Acta Biomater. 2024;185:336–49.
28. Luo H, Wang Z, Yu F, Zhou Z, Wang J, Chen D, Feng Q, Cao X. Adv Funct Mater. 2024;34:2315592.
29. Zhang Y, Shi J, Ma B, Zhou YN, Yong H, Li J, Kong X, Zhou D. Prog Polym Sci. 2023;146;101751.
30. Eusébio D, Neves AR, Costa D, Biswas S, Alves G, Cui Z, Sousa Â. Drug Discov Today. 2021;26:2575–92.
31. Su T, Liu X, Lin S, Cheng F, Zhu G. Bioact Mater. 2023;26:169–80.
32. Kapałczyńska M, Kolenda T, Przybyła W, Zajączkowska M, Teresiak A, Filas V, Ibbs M, Bliźniak R, Łuczewski Ł, Lamperska K. 2D and 3D cell cultures - a comparison of different types of cancer cell cultures. Arch Med Sci. 2018;14(4):910–9.
33. Wang P, Zhang L, Xie Y, Wang N, Tang R, Zheng W, Jiang X. Adv Sci. 2017;4:1700175.
34. Chen X, Zhu Q, Xu X, Shen S, Zhang Y, Mo R. Small 2019;15e1902998.
35. Lv J, Fan Q, Wang H, Cheng Y. Biomaterials. 2019;218:119358.
36. Scholz C, Wagner E. J Control Release. 2012;161:554–65.
37. Liu C, Wan T, Wang H, Zhang S, Ping Y, Cheng Y. Sci Adv. 2019;5:eaaw8922.
38. Kaup R, Ten Hove JB, Velders AH. ACS Nano. 2021;15(1):1666–16746.
39. Chen J, Zhu H, Xia J, Zhu Y, Xia C, Hu Z, Jin Y, Wang J, He Y, Dai J, Hu Z. Adv Sci. 2023;10:e2206306.
40. Yan Y, Zhou L, Sun Z, Song D, Cheng Y. Bioact Mater. 2022;7:333–40.
41. Lee S, Seok BG, Lee SJ, Chung SW. Cell Death Dis. 2022;13;127.
42. Chen X, Zhang A, Zhao K, Gao H, Shi P, Chen Y, Cheng Z, Zhou W, Zhang Y. Ageing Res Rev. 2024;98:102323.
43. Wang D, Zheng H, Zhou W, Duan Z, Jiang S, Li B, Zheng X, Jiang L. Orthop Surg. 2022;14:1569–82.
44. Brunet A, Sweeney LB, Sturgill JF, Chua KF, Greer PL, Lin Y, Tran H, Ross SE, Mostoslavsky R, Cohen HY, Hu LS, Cheng HL, Jedrychowski MP, Gygi SP, Sinclair DA, Alt FW, Greenberg ME. Science. 2004;303;2011–2015.
45. You W, Li Y, Liu K, Mi X, Li Y, Guo X, Li Z. Neural Regen Res. 2024;19;754.
46. Wang H, Zhang C, Li M, Liu C, Wang J, Ou X, Han Y. Int J Mol Sci. 2022;23;12732.
47. Zhang S, Liu W, Chen S, Wang B, Wang P, Hu B, Lv X, Shao Z. Cell Tissue Res. 2022;390:1–22.
48. Zhou X, Shen N, Tao Y, Wan J, Xia K, Ying L, Zhang Y, Huang X, Hua J, Liang C, Chen Q, Li F. Biofabrication. 2023;15:025008.
49. Zhang T, Ding S, Wang R. Int J Mol Sci. 2021;22:10866.
50. Zhou K, Ran R, Gong C, Zhang S, Ma C, Lv J, Lei Z, Ren Y, Zhang H. Pathol Res Pract. 2023;248;154685.
51. Peng Y, Qing X, Shu H, Tian S, Yang W, Chen S, Lin H, Lv X, Zhao L, Chen X, Pu F, Huang D, Cao X, Shao Z. Biomater Transl. 2021;2(2):91–142.
52. Liu Z, Fu C. Front Bioeng Biotechnol. 2022;10:1058251.
53. Le Gal K, Schmidt EE, Sayin VI. Antioxidants. 2021;10;1377.
54. Xu W, Luo FQ, Tong QS, Li JX, Miao WM, Zhang Y, Xu CF, Du JZ, Wang J. CCS Chem. 2021;3:431–42.
55. Sun L, Fang J. Cell Cycle. 2016;15:2647–55.
56. Chen Z, Bai J, Li X, Chen X, Li Z, Pan H, Li S, Gao Q, Zhao N, Chen A, Xu H, Wen Y, Du L, Yang M, Zhou X, Huang J. ACS Nano. 2023;17:25377–90.
57. Liu S, Zhang T, Li S, Wu Q, Wang K, Xu X, Lu M, Shao R, Zhao W, Liu H. Small 2023;19e2206503.
58. Feng D, Kang X, Wang R, Chen H, Zhang K, Feng W, Li H, Zhu Y, Wu S. J Biol Chem. 2020;295:13640–50.
59. Alvarez-Garcia O, Matsuzaki T, Olmer M, Miyata K, Mokuda S, Sakai D, Masuda K, Asahara H, Lotz MK. Aging Cell. 2018;17e12800.
60. Chen S, Liu S, Ma K, Zhao L, Lin H, Shao Z. Osteoarthritis Cartilage. 2019;27:1109–17.
61. Sao K, Risbud MV. Matrix Biol. 2024;131:46–61.
62. Zhou H, Qian Q, Chen Q, Chen T, Wu C, Chen L, Zhang Z, Wu O, Jin Y, Wang X, Guo Z, Sun J, Zhang J, Shen S, Wang X, Jones M, Khan MA, Makvandi P, Zhou Y, Wu A. Small. 2023;20e2308167.
63. Yang Y, Liu Y, Wang Y, Chao Y, Zhang J, Jia Y, Tie J, Hu D. Front Immunol. 2022;13;831168.
64. Liao H, Huang J, Liu J, Zhu H, Chen Y, Li X, Wen J, Yang Q. Mol Biol Rep. 2023;50:3317–27.
65. Gao J, Zhang H, Yang Y, Tao J. Inflammation. 2023;46:835–52.
66. Liu L, Wang W, Huang L, Xian Y, Ma W, Fan J, Li Y, Liu H, Zheng Z, Wu D. Biomaterials 2024;306;122509.
67. Park SH, Kim RS, Stiles WR, Jo M, Zeng L, Rho S, Baek Y, Kim J, Kim MS, Kang H. Choi HS Adv Sci. 2022;9e2200872.
68. Deng S, Zhu F, Dai K, Wang J, Liu C. Biomater Transl. 2023;4:270–9.
69. Chen L, Yang J, Cai Z, Huang Y, Xiao P, Chen H, Luo X, Huang W, Cui W, Hu N. Research 2024;7;0306,.
70. Yang J, Fatima K, Zhou X, He C. Biomater Transl. 2024;5:69–83.
71. Cacciamali A, Villa R, Dotti S. Front Physiol. 2022;13;836480.
72. Jia S, Yang T, Gao S, Bai L, Zhu Z, Zhao S, Wang Y, Liang X, Li Y, Gao L, Zhang Z, Gao X, Li D, Chen S, Zhang B, Meng C. J Orthop Translat. 2024;46:103–15.
73. Ohnishi T, Iwasaki N, Sudo H. Cells. 2022;11(3):394.

Publisher's note